

Developing novel high-temperature soft-magnetic B2-based multi-principal-element alloys with coherent body-centered-cubic nanoprecipitates

Zhenhua Wang ^a, Junhao Yuan ^a, Qing Wang ^{a,*}, Zhen Li ^b, Xuyang Zhou ^c, Junhua Luan ^d, Jing Wang ^e, Shijian Zheng ^e, Zengbao Jiao ^{f,*}, Chuang Dong ^a, Peter. K. Liaw

^g

^a *Key Laboratory of Materials Modification by Laser, Ion and Electron Beams (Ministry of Education), School of Materials Science and Engineering, Dalian University of Technology, Dalian 116024, China*

^b *School of Mechanical Engineering, Dalian University of Technology, Dalian 116024, China*

^c *Max-Planck-Institut für Eisenforschung, Max-Planck-Straße 1, Düsseldorf 40237, Germany*

^d *Inter-University 3D Atom Probe Tomography Unit, Department of Materials Science and Engineering, City University of Hong Kong, Hong Kong, China*

^e *State Key Laboratory of Reliability and Intelligence of Electrical Equipment, Hebei University of Technology, Tianjin 300130, China*

^f *Department of Mechanical Engineering, Research Institute for Advanced Manufacturing, The Hong Kong Polytechnic University, Hong Kong, China*

^g *Department of Materials Science and Engineering, University of Tennessee, Knoxville, Tennessee 37996, USA*

*Corresponding authors. Tel./Fax: +86-411-84708615. E-mail addresses: wangq@dlut.edu.cn (Q. Wang), zb.jiao@polyu.edu.hk (Z.B. Jiao).

ABSTRACT

Multi-principal-element alloys (MPEAs) have attracted considerable attention due to their enhanced possibilities of obtaining superior properties by tailoring chemical compositions in an enormous space. This work developed a series of novel soft-magnetic MPEAs via the cluster formula approach of $\text{Al}_3(\text{Co,Fe,Cr})_{14}$. Through deliberately manipulating their microstructures, ultrafine ferromagnetic body-centered-cubic (BCC) nanoparticles (3 ~ 8 nm in diameter) are coherently precipitated in a B2 matrix. These alloys exhibit a high saturation magnetization of 107.4 ~ 167.5 emu/g and a low coercivity of 143 ~ 303 A/m in the homogenized and aged states. Even after aging for 480 h at 873 ~ 1073 K, the prominent soft-magnetic properties can still be retained, which can be ascribed to the excellent stability of the coherent BCC/B2 microstructure. Importantly, these materials also show excellent soft-magnetic properties at high temperatures. The $\text{Al}_3\text{Co}_7\text{Fe}_7$ alloy exhibits a saturation magnetization of 134.7 emu/g and a coercivity of 167.2 A/m at 973 K. Moreover, they have high Curie temperatures (1254 K for $\text{Al}_3\text{Co}_7\text{Fe}_7$ and 1052 K for $\text{Al}_3\text{Co}_6\text{Fe}_6\text{Cr}_2$) and electrical resistivity (262 ~ 285 $\mu\Omega\cdot\text{cm}$). The outstanding high-temperature magnetic properties of the presently developed alloys is discussed in light of the microstructural stability and evolution with chemical composition and temperature and the coercivity is found to be closely related to the particle size of BCC nanoprecipitates. With the advantages of the currently developed BCC/B2 MPEAs over conventional soft-magnetic alloys, the coherent precipitation approach opens a new way to design novel high-temperature soft-magnetic materials.

Keywords: multi-principal-element alloys; soft-magnetic properties; coherent precipitation; microstructural stability

1. Introduction

Soft-magnetic materials with high saturation magnetization (or saturation induction intensity) and permeability as well as low coercivity have been widely applied in power generation, electronic, and aerospace fields [1, 2]. Commercial soft-magnetic alloys, such as Fe-(3~4.5)Si and Fe-(30~50)Co (weight percent, wt.%) alloys, are prevalent among industries due to their high saturation magnetization ($B_S = 1.9 \sim 2.4$ T) and low coercivity ($H_C < 150$ A/m) [3, 4]. Nevertheless, their low electrical resistivity ($\rho < 50 \mu\Omega \cdot \text{cm}$) leads to a high eddy current loss, limiting their applications in high-frequency fields. Fe- and Co-based amorphous/nanocrystalline alloys have high electrical resistivity of $100 \sim 150 \mu\Omega \cdot \text{cm}$ due to their random atomic packing in a long range [5-9]. Meanwhile, this kind of alloys possess high B_S (1.2 ~ 2.0 T) and low H_C (< 10 A/m), which is ascribed mainly to the uniform distribution of ultrafine ferromagnetic body-centered-cubic (BCC) nanoprecipitates (less than 20 nm) in the amorphous matrix, as exemplified by the Fe-based Finemet $\text{Fe}_{73.5}\text{Si}_{13.5}\text{Nb}_3\text{B}_9\text{Cu}_1$ (atomic percent, at.%) alloy with $B_S = 1.2$ T and $H_C = 0.5$ A/m [9]. However, the metastable nature of the amorphous matrix limits their high-temperature (HT) applications to the service temperatures below 573 K (the Curie temperature $T_C \sim 850$ K) [7, 9]. The partial substitution of Co for Fe can increase the B_S , H_C , and T_C , as evidenced by the values of $B_S = 2.0$ T, $H_C = 160$ A/m, and $T_C = 1253$ K in Hitperm $\text{Fe}_{44}\text{Co}_{44}\text{Zr}_7\text{B}_4\text{Cu}_1$ (at. %) alloy [8]. Moreover, this series of alloys have the largest resistivity ($\rho \sim 150 \mu\Omega \cdot \text{cm}$) among all existing conventional soft-magnetic alloys [8].

Similarly, multi-principal-element alloys (MPEAs), also known as high- and medium-entropy alloys (H/MEAs), possess high electrical resistivity due to the long-range-disordered occupations of atoms on lattice sites [10-14]. In sharp contrast to traditional practice, the high-entropy alloying strategy has attracted much attention

since it can endow MPEAs with both prominent mechanical and functional properties, including the corrosion/oxidation resistance, irradiation resistance, magnetic properties, electromagnetic wave-absorption, thermoelectric properties, etc. [12-17]. For instance, the $\text{Co}_{27.7}\text{Fe}_{32.6}\text{Ni}_{27.7}\text{Ta}_{5.0}\text{Al}_{7.0}$ (at. %) MPEA possesses fascinating mechanical and soft-magnetic properties (a tensile yield strength of 904 MPa, saturation magnetization of 100 emu/g, coercivity of 78 A/m, electronic resistivity of $103 \mu\Omega\cdot\text{cm}$, and Curie temperature of 694 K), which were ascribed to the special microstructure composed of the ferromagnetic face-centered-cubic (FCC) matrix and paramagnetic coherent L1_2 nanoprecipitates [17]. It is noted that any crystalline defects (grain boundaries, phase boundaries, dislocations, solute elements, etc.) to strengthen alloys would impede the movement of magnetic domains through pinning the domain walls, leading to an increase in coercivity [18-20]. For instance, the coercivity of the $\text{Co}_{27.7}\text{Fe}_{32.6}\text{Ni}_{27.7}\text{Ta}_{5.0}\text{Al}_{7.0}$ alloy is strongly dependent on the particle size of coherent precipitates. As the average particle size increases from 24 to 91 nm, the coercivity decreases from 763 to 78 A/m, because the coherent stress characterized by the specific surface area and lattice misfit between the matrix and nanoprecipitates with a small particle size is higher than that with a medium particle size [17, 18]. If the particle size of nanoprecipitates is comparable to or slightly larger than the magnetic domain wall width, the coercivity might increase drastically and the soft-magnetic feature would disappear.

Extensive reports have demonstrated that the saturation magnetization is dependent on the concentration of ferromagnetic elements (Fe, Co, and Ni), while the saturation magnetization, coercivity, and electrical resistivity are primarily controlled by the microstructure, including the phase constitution and morphology [18]. In particular, the coercivity, as the fundamental parameter for soft magnetism, is closely related to the size of ferromagnetic precipitates in nanocrystalline alloys or the grain

size in conventional polycrystalline alloys [18]. MPEAs open a new avenue to design novel soft-magnetic alloys, since their microstructures are highly tunable and can be well-controlled by optimizing the chemical compositions in an enormous space. For instance, the FCC-FeCoNi alloy exhibits an extremely-high saturation magnetization of 155.7 emu/g and low coercivity of 189 A/m [21], but further alloying with Al and Mn would deteriorate the soft-magnetic properties, as evidenced by the BCC/B2 FeCoNiMnAl alloy ($M_S = 132.2$ emu/g and $H_C = 266$ A/m) and the dual-phase FeCoNiMn_{0.5}Al_{0.5} alloy with an FCC + BCC/B2 structure ($M_S = 51.9$ emu/g and $H_C = 730$ A/m) [21]. Recently, we developed a soft-magnetic Al_{1.5}Co₄Fe₂Cr alloy via the cluster-formula approach with the formula of Al₃M₁₄ (M₁₄ = Co₈Fe₄Cr₂), which exhibits a saturation magnetization of 135.3 emu/g, coercivity of 127.3 A/m, Curie temperature of 1061 K, and electrical resistivity of 244 $\mu\Omega\cdot\text{cm}$ [13]. The outstanding soft-magnetic properties are ascribed to its unique coherent microstructure with ultrafine, spherical, and ferromagnetic BCC nanoprecipitates with a size of 3 ~ 7 nm uniformly distributed in a B2 matrix. However, when the BCC/B2 coherent microstructure was reversed, i.e., large-sized cuboidal B2 nanoparticles (~100 nm) in the BCC matrix in an Al_{0.7}NiCoFeCr₂ alloy designed with the cluster formula of Al₂M₁₄, the soft-magnetic properties deteriorate seriously ($M_S = 28.9$ emu/g and $H_C = 947$ A/m). When a weave-like BCC/B2 microstructure appears in an Al_{0.57}NiCoFeCr (Al₂M₁₄) alloy, the soft-magnetic feature almost vanishes due to the extremely-high coercivity (4035 A/m) and extremely-low saturation magnetization (11.7 emu/g) [13]. These results demonstrated that the magnetic properties of MPEAs are strongly dependent on the microstructure. More importantly, considering that the BCC/B2-structured MPEAs offer great potential for applications as HT soft magnets, the influence of microstructural evolution of the

BCC/B2 coherent structure on the soft-magnetic properties should be further explored in detail.

In the present work, we applied the cluster formula of Al_3M_{14} to design a new series of MPEAs in the Al–Co–Cr–Fe system, where M can be tailored and represents different combinations of Co, Cr, and Fe. The cluster formula approach has been successfully applied to design alloy compositions in multi-component systems, in which the alloying elements could be rationally matched and thus the amount of each element could be optimized [13, 22, 23]. More significantly, the BCC/B2 coherent microstructure with spherical or cuboidal nanoprecipitates could be well controlled via the cluster formula in Al-TMs (transition metals) alloys to achieve prominent mechanical and functional properties simultaneously. For example, the $\text{Al}_2\text{Ti}_6\text{Zr}_2\text{Nb}_3\text{Ta}_3$ (Al_2M_{14}) alloy has both a high yield strength (1193 MPa) and an ultrahigh combustion calorific capacity ($10240 \text{ J}\cdot\text{g}^{-1}$), showing a great potential to be used as novel energetic structural materials [24, 25]. Besides, the soft-magnetic $\text{Al}_{1.5}\text{Co}_4\text{Fe}_2\text{Cr}$ alloy also exhibits a high yield strength of 1200 MPa [13]. Here, Ni is removed in order to form Fe/Co-rich BCC nanoparticles to maximize the saturation magnetization since the magnetic moment (μ_H) of Ni is smaller than that of Fe and Co ($\mu_{H,Fe} = 2.2\mu_B$, $\mu_{H,Co} = 1.7\mu_B$, and $\mu_{H,Ni} = 0.6\mu_B$, μ_B is the Bohr magneton) [26]. Meanwhile, a proper addition of Al via the cluster formula of Al_3M_{14} can avoid the formation of weave-like BCC/B2 microstructure [13, 27, 28]. Cr is introduced because it has the potential to tailor the lattice misfit between the BCC and B2 phases for the formation of ultrafine spherical nanoprecipitates [26-28]. Under the above considerations, five MPEAs were designed, i.e., S1- $\text{Al}_3\text{Co}_7\text{Fe}_7$, S2- $\text{Al}_3\text{Co}_6\text{Fe}_7\text{Cr}_1$, S3- $\text{Al}_3\text{Co}_6\text{Fe}_6\text{Cr}_2$, S4- $\text{Al}_3\text{Co}_7\text{Fe}_4\text{Cr}_3$, and S5- $\text{Al}_3\text{Co}_4\text{Fe}_7\text{Cr}_3$. Table 1 lists their chemical compositions. The microstructures and magnetic properties of these alloys in different

states were systematically characterized, aiming at understanding the influence of chemical compositions and microstructural evolution (including phase constitution and particle morphology) on the soft-magnetic properties of the alloys. The microstructural dependence of coercivity and the compositional dependence of saturation magnetization were discussed, and the electrical resistivity of these alloys at both room temperature (RT) and HTs were analyzed. Emphases were placed on revealing the correlation of microstructural evolution and stability of the coherent BCC/B2 structure with the soft-magnetic properties at HTs.

2. Experimental

The $\text{Al}_3(\text{Co,Fe,Cr})_{14}$ MPEA samples were prepared by means of arc melting and suction-casting into a copper mold with a dimension of $2 \text{ mm} \times 9 \text{ mm} \times 60 \text{ mm}$ under an argon atmosphere. The purity of raw metals is better than 99.99 wt. %. Alloy ingots with a weight of about 10 g were re-melted at least five times to ensure chemical homogeneity followed by suction-casting. These alloy plates were homogenized at 1573 K for 2 h and then aged for 24 h at different temperatures (773, 873, 973, and 1073 K). Particularly, some representative alloys were selected for aging at 873 ~ 1073 K for 480 h to study the thermal stability of the microstructure. Water quenching was done for all heat treatment cycles.

Crystal structures of both homogenized and aged alloys were examined using a Bruker D8 X-ray diffractometer (XRD) with a $\text{Cu-K}\alpha$ radiation ($\lambda = 0.15406 \text{ nm}$) at a scanning speed of $2^\circ/\text{min}$, in which an external standard method was applied to calculate the lattice constants of phases [29]. The microstructures were examined using a Zeiss Supra 55 scanning electron microscope (SEM) and JEOL-JEM-2100F field-emission transmission electron microscope (TEM). An aberration-corrected JEM-

ARM300F TEM equipped with an energy dispersive spectroscopy (EDS) detector was used to analyze the morphology of ultrafine nanoprecipitates and elemental distribution. Electron backscatter diffraction (EBSD) measurements were performed using the JEOL-JSM-IT800SHL SEM, where the samples were prepared by argon ion beam polishing. Samples for SEM observations were mechanically ground, polished, and then etched in a solution consisting of 5 g $\text{FeCl}_3 \cdot 6\text{H}_2\text{O}$, 25 ml HCl, and 25 ml $\text{C}_2\text{H}_5\text{OH}$. TEM specimens were prepared by an FEI Helios NanoLab 600 Dual-Beam focused ion beam (DB-FIB) instrument and the detailed procedure was described elsewhere [30]. Atom probe tomography (APT) characterizations were performed in a local electrode atom probe (CAMEACA LEAP 5000 XR). Needle-shaped specimens were fabricated by lift-outs and annular milled in a FEI Scios FIB/SEM, and the specimens were analyzed at 70 K in voltage mode with a pulse repetition rate of 200 kHz, a pulse fraction of 20 %, and an evaporation detection rate of 0.2 % atom per pulse [31]. The data analysis workstations AP Suite 6.1 was used for the 3D reconstructions and data analyses [32].

The saturation magnetization and coercivity of the alloys in different states at both RT and HTs (873 and 973 K) were measured with a vibrating sample magnetometer (VSM, Lake Shore 7410) under a maximum applied field of 15000 Oe. Curie temperatures were also measured with the VSM from 375 to 1123 K under an applied field of 10000 Oe. The electrical resistivity of these alloys at RT and HTs was measured with a variable temperature-resistivity meter (TRT-1000), in which the testing temperature increased from RT to 1073 K with a constant heating rate of 10 K/min (testing at every 50 K interval).

3. Results

3.1 Soft-magnetic properties in different states

Room-temperature hysteresis loops of the designed $\text{Al}_3(\text{Co,Fe,Cr})_{14}$ MPEAs in the homogenized state are shown in Fig. 1a, from which the magnetic properties, including the saturation magnetization and coercivity, were estimated and are listed in Table 1. It can be seen that this series of alloys exhibit good soft-magnetic properties with saturation magnetization of 107.4 ~ 167.5 emu/g and coercivity of 143 ~ 303 A/m (1.8 ~ 3.8 Oe). Specifically, with increasing the Cr content, the saturation magnetization is reduced gradually from 167.5 to 107.4 emu/g. Among them, the S1- $\text{Al}_3\text{Co}_7\text{Fe}_7$ alloy without Cr additions has the largest saturation magnetization value. The coercivity does not show significant changes among different alloys, but all values are at a considerably low level, showing a good soft-magnetic feature.

To investigate the influence of aging temperature on the soft-magnetic properties, the S1- $\text{Al}_3\text{Co}_7\text{Fe}_7$, S3- $\text{Al}_3\text{Co}_6\text{Fe}_6\text{Cr}_2$, and S5- $\text{Al}_3\text{Co}_4\text{Fe}_7\text{Cr}_3$ alloys were aged for 24 h at different temperatures ranging from 773 to 1073 K. The hysteresis loops of the aged alloys at different temperatures are shown in Figs. 1b–d, and the saturation magnetization and coercivity values are also listed in Table 1. It is found that the soft-magnetic properties of the S1- $\text{Al}_3\text{Co}_7\text{Fe}_7$ alloy are not sensitive to the aging temperature, still showing a high saturation magnetization of 160 ~ 165 emu/g and a low coercivity of 151 ~ 183 A/m (1.9 ~ 2.3 Oe), which are comparable to those ($M_S = 167.5$ emu/g and $H_C = 191.0$ A/m) in the homogenized state. Although the saturation magnetization of the aged S3- $\text{Al}_3\text{Co}_6\text{Fe}_6\text{Cr}_2$ alloy remains unchanged (~ 129 emu/g), its coercivity increases slightly with the aging temperature, as evidenced by the coercivity of 150 A/m (1.9 Oe) in the 773 ~ 873-K aged states and 270 ~ 374 A/m (3.4 ~ 4.7 Oe) in the 973 ~ 1073-K aged states. However, for the S5- $\text{Al}_3\text{Co}_4\text{Fe}_7\text{Cr}_3$ alloy, the coercivity increases drastically after aging at HTs, showing the coercivity of 811.9 A/m (10.2 Oe)

in the 973-K aged state and 1974 A/m (24.8 Oe) in the 1073-K aged state, which indicates that there might occur a remarkable variation in microstructure. Moreover, it is emphasized that the saturation magnetization values of these alloys are not affected by the aging temperature, confirming that the saturation magnetization is closely related to the amount of ferromagnetic elements, rather than the microstructures [18]. Resultantly, the low saturation magnetization (103 ~ 111 emu/g) of S5 can be ascribed to the increase of non-ferromagnetic Cr content (17.65 at.%).

Furthermore, both the S1-Al₃Co₇Fe₇ and S3-Al₃Co₆Fe₆Cr₂ alloys were aged at 873 ~ 1073 K for a long time of 480 h, and their magnetic properties were also measured, as presented in Figs. 1b and c and Table 1. Fascinatingly, even after a long-term aging at 973 ~ 1073 K, the S1 alloy still shows excellent soft-magnetic properties with a high saturation magnetization (157.9 ~ 165.4 emu/g) and a low coercivity (135.3 ~ 183.1 A/m or 1.7 ~ 2.3 Oe). While the long-term aging at 973 K deteriorates the soft-magnetic properties of the S3 alloy, leading to an increase of the coercivity to 1950.2 A/m (24.5 Oe). By contrast, the S3 alloy still exhibits prominent soft-magnetic properties with a moderate saturation magnetization of 132.0 emu/g and a low H_C of 159.2 A/m (2.0 Oe) after a long-term aging at 873 K.

3.2 Microstructure in different states

3.2.1 In the homogenized state

To understand the influence of heat treatments on the soft-magnetic properties of the Al₃(Co,Fe,Cr)₁₄ MPEAs, we executed a detailed characterization on phase constitutions and microstructural morphologies of the alloys. Figure 2a displays the XRD patterns of the as-homogenized alloys. It is evident that all these alloys consist of disordered BCC solid solution and ordered B2 phases (characterized by the (100) diffraction peak). The lattice constants of the BCC and B2 phases were measured, and their lattice misfit ε

were calculated by $\varepsilon = 2 \times (a_{B2} - a_{BCC}) / (a_{B2} + a_{BCC})$, where a_{BCC} and a_{B2} are the lattice constants of the BCC and B2 phases, respectively, as listed in Supplementary Table S1. Figure 2b shows the variations of lattice constants of the BCC and B2 phases and their lattice misfits with the Cr content. It is found that the lattice misfits in these as-homogenized alloys decrease slightly with the increased Cr addition, being in the range of 0.14% ~ 0.21%. It is noted that all these lattice misfit values are relatively smaller as compared with those ($\varepsilon = 0.2\% \sim 0.6\%$) in previously reported Al-Ni-Co-Fe-Cr MPEAs containing the coherent BCC/B2 precipitation [22].

Microstructures of these homogenized MPEAs were characterized by the EBSD, SEM, and TEM. Figures 3a and b show the EBSD inverse pole figure (IPF) maps of the S1-Al₃Co₇Fe₇ and S3-Al₃Co₆Fe₆Cr₂ alloys. Both alloys contain coarse equiaxed grains with an average size of 200 ~ 400 μm , and within the grains there are micro-scale cells with a size of 120 ~ 400 nm, as illustrated in Figs. 3c and d. Supplementary Fig. S1 shows the elemental mapping obtained from STEM-EDS analysis, which suggests that the formation of micro-scale cells can be ascribed to the segregation of Co and Fe on the cell boundaries. Interestingly, the TEM analysis indicates that in the cell interior of the S3 alloy, spheroidal BCC nanoparticles with a diameter of 3 ~ 5 nm are coherently precipitated in the ordered B2 matrix, as presented in the dark-field (DF) image and corresponding selected-area electron diffraction (SAED) pattern (Fig. 3e). High-resolution TEM (HRTEM) along the [100] direction and the fast Fourier transformation (FFT) patterns reveal more details on the BCC nanoprecipitates (red arrows in Fig. 3f), demonstrating that the BCC nanoprecipitates are perfectly coherent with the B2 matrix. Therefore, this series of MPEAs have a hierarchical microstructure, consisting of macro-scale equiaxed grains, micro-scale cells, and nano-scale precipitates. Particularly, the formation of spherical nanoprecipitates should be

attributed to the small lattice misfit ($\varepsilon < 0.2\%$) between the coherent BCC and B2 phases, since a large lattice misfit would generally result in the precipitation of plate- or needle-like nanoprecipitates or the formation of a weave-like spinodal microstructure [22].

3.2.2 In the aged states

After aging at different temperatures, the sizes of both macro-scale grains and micro-scale cells do not show significant changes, which are comparable to those in the as-homogenized samples. For the S1-Al₃Co₇Fe₇ alloy, even after a long-term aging for 480 h at 973 ~ 1073 K, the micro-scale cells do not coarsen significantly and show an average cell size of 300 ~ 400 nm, as presented in Fig. 4. Notably, the BCC nanoprecipitates are not susceptible to both aging temperature and time. Figure 5a shows the TEM analysis of the S1 alloy after aging at 773 K for 24 h. The DF-TEM image and corresponding SAED pattern along the [110]_{BCC} direction indicate that the ultrafine BCC nanoparticles with a size of 3 ~ 8 nm are precipitated in the L₂₁ matrix. Here, L₂₁ is a highly-ordered BCC-derived phase, which consists of eight lattice cells of ordered B2 structures [33]. When the S1 alloy was aged at 973 and 1073 K for 480 h, the TEM-DF and HAADF images confirm that the ultrafine BCC nanoparticles with a size of 3 ~ 8 nm are still coherent with the B2 matrix, as shown in Figs. 5b and c. Furthermore, the compositional analysis of the BCC nanoprecipitates and B2 matrix by using TEM-EDS are presented in Fig. 5d. The average compositions of the BCC nanoprecipitates and B2 matrix are Al_{13.1}Co_{45.7}Fe_{41.2} and Al_{15.7}Co_{43.0}Fe_{41.3} (at.%), respectively, showing only a small composition difference between these two phases. For the L₂₁ matrix in the 773-K aged state, it could be understood by the phase transformation from the B2 to L₂₁ structure [34]. In the Fe-Al binary phase diagram

[35], there exists a L2₁-Fe₃Al phase at 673 ~ 850 K, and the B2 phase can transform to the L2₁ phase at an Al content of ~ 20 at.% at elevated temperatures.

To further study the elemental partitioning between the BCC nanoprecipitates and B2 matrix, we applied the APT technique to analyze the S1 alloy after aging at 1073 K for 480 h. Figure 6a shows the atom maps of Al, Co, and Fe, in which the relative position and extent of Al (green), Co (blue), and Fe (red) are indicated. It appears that Co exhibits a slight segregation. For statistical analysis, the concentration isosurface of 44 at.% Co was used to visualize the Co-enriched precipitates (Fig. 6b), based on which the corresponding proximity histogram is displayed in Fig. 6c. It is found that the average size of the nanoprecipitates is 2.1 ± 1.4 nm. Moreover, Al and Fe are enriched in the B2 matrix, and Co partitions to the BCC nanoprecipitates, which is consistent with the TEM-EDS results (Fig. 5e). In other words, there exists a slight difference in composition between these two phases. Therefore, the BCC/B2 coherent microstructure in the S1-Al₃Co₇Fe₇ alloy has a high thermal stability at HTs up to 1073 K, which contributes to the prominent soft-magnetic properties, as evidenced by the high saturation magnetization of 157.9 emu/g and low coercivity of 135.3 A/m or 1.7 Oe (Fig. 1b).

For the S3-Al₃Co₆Fe₆Cr₂ alloy, the SEM micrographs after aging at 973 K for 24 and 480 h are shown in Fig. 7. In the 24-h aged state, the particle size (~ 90 nm) of BCC nanoprecipitates in the B2 matrix is obviously larger than that (~ 5 nm) in the as-homogenized state (Figs. 3e and f). These BCC nanoprecipitates coarsen remarkably after aging for 480 h (Fig. 7b). Multiple BCC nanoprecipitates are merged into coarse ellipsoidal particles with an ellipsoidal shape, showing a size of ~ 150 nm or short-rod particles with a length of ~ 500 nm and a width of ~ 190 nm. Moreover, the 480-h aged sample was characterized by STEM, and the HAADF-STEM image and corresponding

TEM-EDS mapping of the BCC and B2 phases are shown in Fig. 8. Obviously, the B2 matrix is enriched in Al and Fe, whereas Co and Cr partition mainly to the BCC nanoprecipitates. The coarsening of BCC nanoprecipitates increases the coercivity gradually up to 1950 A/m in 480-h aged state (Fig. 1c and Table 1). Accordingly, the soft-magnetic properties of the 773 ~ 873-K aged samples are similar to those of the homogenized sample, which implies that the microstructure in the aged state is similar to that in the homogenized state (Figs. 3e and f), i.e., the uniform distribution of ultrafine BCC nanoprecipitates in the B2 matrix.

Furthermore, APT was also applied to study the elemental distribution and particle morphology in the S3-Al₃Co₆Fe₆Cr₂ alloy after aging at 773 K for 24 h. Figure 9a shows the atom maps of Al, Cr, Fe, and Co, from which the non-uniform distribution of Cr can be clearly identified. The morphology of the Cr-enriched regions was further visualized by the concentration isosurface (green) of 25 at.% Cr in an enlarged view, as presented in Fig. 9b. Fe is slightly enriched at the interface between the Cr-enriched particle and matrix, as evidenced by the concentration isosurface (red) of 39 at.% Fe. Figure 9c shows the corresponding proximity histogram to quantify the elemental distributions across the interface between the Cr-enriched nanoprecipitates and matrix, from which the Fe segregation at the nanoprecipitate-matrix interface was clearly observed (marked by the red arrow). That is, the non-ferromagnetic Cr-enriched nanoprecipitates is surrounded by the ferromagnetic Fe to form composite nanoprecipitates with composition gradients. The average size and number density of the nanoprecipitates are 3.1 ± 1.3 nm and 3.2×10^{21} m⁻³, respectively. The formation of such composite BCC nanoprecipitates might be attributed to the fast diffusion of Cr and the preferred Cr-Fe segregation in BCC-based alloys, which was previously observed in Fe-Cr-Al-based ferritic stainless steels [36].

The SEM micrographs of the S5-Al₃Co₄Fe₇Cr₃ alloy after aging for 24 h at different temperatures are presented in Fig. 10. It is seen that in the 773-K and 873-K aged states, the micro-scale cell boundaries still exist (Figs. 10a and b). With the increase of aging temperature, these BCC nanoprecipitates coarsen markedly, as evidenced by the cuboidal particles with a size of 300 ~ 500 nm in 973-K aged state (Fig. 10c) and a BCC/B2 lamellar microstructure with a width of ~ 180 nm in 1073-K aged state (Fig. 10d). Notably, the coarsening of BCC nanoprecipitates after aging at 973 ~ 1073 K deteriorates the soft-magnetic properties of the S5 alloy drastically, as demonstrated by saturation magnetization of 114.5 emu/g and coercivity of 119.4 A/m (1.5 Oe) in the 773-K aged state and saturation magnetization of 108.1 emu/g and coercivity of 1974.1 A/m (24.8 Oe) in the 1073-K aged state (Fig. 1d).

3.3 Curie temperature and HT soft-magnetic properties

In view of the high thermal stability of the coherent BCC/B2 microstructure the S1-Al₃Co₇Fe₇ and S3-Al₃Co₆Fe₆Cr₂ alloys, it is significant to evaluate their Curie temperature and HT soft-magnetic properties. Figures 11a and b show the thermomagnetic curves of these two alloys, from which the Curie temperature were estimated, being 1254 and 1052 K for the S1 and S3 alloys, respectively. The former is higher than the latter, indicating that the addition of non-ferromagnetic Cr decreases the Curie temperature. The HT hysteresis loops of these two 973-K aged samples were measured at 773 ~ 973 K, and the results are presented in Figs. 11c and d. The measured values of the Curie temperature (T_C), saturation magnetization (M_S), and coercivity (H_C) are listed in Table 2. More significantly, the soft-magnetic properties of the S1-Al₃Co₇Fe₇ alloy are not sensitive to testing temperature, still showing a high saturation magnetization of 134 ~ 151 emu/g and a low coercivity of 167 ~ 191 A/m or 2.1 ~ 2.3 Oe at HTs up to 973 K. Especially, the coercivity values at HTs are comparable to that

(159.2 A/m or 2.0 Oe) at RT, while the saturation magnetization at HTs is slightly lower than that (162.8 emu/g) at RT. By contrast, the saturation magnetization of the S3- $\text{Al}_3\text{Co}_6\text{Fe}_6\text{Cr}_2$ alloy decreases to 104 ~ 115 emu/g at 773 ~ 873 K and to 58.0 emu/g at 973 K, whereas the coercivity increases sharply to 151 A/m (1.9 Oe) at 773 ~ 873 K and to 517.4 A/m (6.5 Oe) at 973 K. Therefore, it can be concluded that the excellent soft-magnetic properties of the S1 alloy can be retained at temperatures up to 973 K, while those of the S3 alloy can be kept at 873 K and below.

3.4 Electrical resistivity

The electrical resistivity is another key characteristic for HT soft-magnetic alloys, and a high electrical resistivity could reduce the eddy current loss according to the inverse relationship between them [25]. Figure 12a shows the electrical resistivity of the five homogenized MPEAs at RT. It is found that all these alloys exhibit relatively high electrical resistivity (262 ~ 285 $\mu\Omega\cdot\text{cm}$) and the resistivity is gradually rising with the amount of non-ferromagnetic Cr. For example, the resistivity of the S1- $\text{Al}_3\text{Co}_7\text{Fe}_7$ alloy is 262 $\mu\Omega\cdot\text{cm}$, while that of the S5- $\text{Al}_3\text{Co}_4\text{Fe}_7\text{Cr}_3$ alloy is 285 $\mu\Omega\cdot\text{cm}$. This can be explained from the high resistance to electron movement from the large lattice distortion due to the addition of Cr [17]. Actually, all these alloys possess high electrical resistivity, much greater than that of Fe-based amorphous and nano-crystalline alloys (80 ~ 150 $\mu\Omega\cdot\text{cm}$) [8, 37]. In addition, the variation of electrical resistivity of the S3- $\text{Al}_3\text{Co}_6\text{Fe}_6\text{Cr}_2$ alloy with the temperature (from RT to 1078 K) was also measured and is shown in Fig. 12b. In the low-temperature region (RT < T < 873 K), the resistivity increases slowly with temperature, being 276 $\mu\Omega\cdot\text{cm}$ at RT and 300 $\mu\Omega\cdot\text{cm}$ at 873 K. While the resistivity increases dramatically in the high temperature region (873 K < T < 1078 K), in which the resistivity increases up to 328 $\mu\Omega\cdot\text{cm}$ at 1078 K. This

incomparable electrical resistivity could surpass that of most HEAs ($100 \sim 300 \mu\Omega\cdot\text{cm}$) [38].

3.5 Comparison of soft-magnetic properties

Generally, soft-magnetic alloys with high electrical resistivity and Curie temperature have a great potential for HT applications. The resistivity (ρ) and Curie temperature (T_C) of the current series of alloys are compared with those of conventional soft-magnetic materials [8, 25, 37-39], including traditional alloys, amorphous alloys, nanocrystalline alloys, and existing MPEAs, as shown in Fig. 13a and Table S2. It is seen that the current series of alloys possess the highest electrical resistivity ($262 \sim 285 \mu\Omega\cdot\text{cm}$), which is almost twice as high as that ($100 \sim 180 \mu\Omega\cdot\text{cm}$) of amorphous and nanocrystalline alloys and five times higher than that of traditional Fe-Si steels ($\rho < 90 \mu\Omega\cdot\text{cm}$). The higher the resistivity, the lower the eddy current loss. In addition, some alloys, such as the current S1- $\text{Al}_3\text{Co}_7\text{Fe}_7$ and S3- $\text{Al}_3\text{Co}_6\text{Fe}_6\text{Cr}_2$, as well as $\text{Al}_{1.5}\text{Co}_4\text{Fe}_2\text{Cr}$ [13] show a Curie temperature of over 1000 K (the purple area in the upper right corner of Fig. 13a), indicating that they have the potential to be used as HT soft-magnets. Furthermore, the S1- $\text{Al}_3\text{Co}_7\text{Fe}_7$ alloy with a supersaturated magnetization of 134.0 emu/g and coercivity of 167.2 A/m at 973 K and the S3- $\text{Al}_3\text{Co}_6\text{Fe}_6\text{Cr}_2$ alloy with a supersaturated magnetization of 104.4 emu/g and coercivity of 151.2 A/m at 873 K demonstrate high potential as candidate materials for HT soft-magnetic applications. Although the Hitperm $\text{Fe}_{44}\text{Co}_{44}\text{Zr}_7\text{B}_4\text{Cu}_1$ (at. %) alloy has a high Curie temperature of 1253 K, the metastable feature of the amorphous matrix confines its service temperature below 800 K [8].

In order to clearly explicit the soft-magnetic properties of the current series of alloys, Fig. 13b gives the saturation induction intensity (B_S) and coercivity (H_C) values of typical soft-magnetic materials, where the data is taken from Refs. [30, 40]. Firstly, the

currently developed S1-Al₃Co₇Fe₇ alloy (red star) have a relatively higher saturation induction intensity and lower coercivity, especially the S1-Al₃Co₇Fe₇ alloy, as compared with most of the existing soft-magnetic MPEAs. In addition, the saturation induction intensity values of the current alloys are comparable to those of amorphous and nanocrystalline alloys, although they are slightly inferior to the traditional Fe-Co and Fe-Si alloys. More importantly, the high-temperature soft-magnetic properties of the current alloys are significantly superior to those of amorphous and nanocrystalline alloys. For instance, the saturation magnetization (150.6 emu/g at 773 K) of the current S1 alloy is much larger than that (13.7 emu/g at 700 K) of Finemet alloy, despite its lower coercivity (0.6 Oe) [40]. Particularly, the high electrical resistivity in the current alloys has never been observed in any of traditional soft-magnetic alloys. Therefore, the currently developed MPEAs are attractive as affordable high-temperature soft-magnets.

4. Discussion

4.1 Composition and temperature dependences of thermal stability of coherent BCC/B2 structures

From the above characterization, it is found that this series of alloys in the homogenized state consist of disordered BCC solid solution and ordered B2 phase (Fig. 2a), and the low lattice misfit (0.14% ~ 0.21%) between the two phases produces the coherent microstructure with ultrafine ferromagnetic BCC nanoparticles (3 ~ 8 nm in size) in the B2 matrix. The coherent BCC/B2 microstructure renders the alloys with prominent and incomparable soft-magnetic properties (saturation magnetization of 107.4 ~ 167.5 emu/g and coercivity 143 ~ 303 A/m). However, it is noted that the microstructural evolutions in these alloys vary with both aging temperature and time.

With increasing the Cr content, the thermal stability of the coherent BCC/B2 microstructure can be reduced gradually. Among them, the coherent microstructure of the S1- $\text{Al}_3\text{Co}_7\text{Fe}_7$ alloy exhibits the highest thermal stability. Even after a long-term aging at 1073 K for 480 h, the ultrafine BCC nanoprecipitates do not coarsen significantly and the particle size (3 ~ 8 nm) is still comparable to that in the homogenized state (Figs. 5b and c). As a result, this alloy exhibits prominent soft-magnetic properties at HTs (saturation magnetization of 134.7 emu/g and 167.2 A/m at 973 K) (Fig. 11c). For the S3- $\text{Al}_3\text{Co}_6\text{Fe}_6\text{Cr}_2$ alloy, the BCC nanoprecipitates show negligible coarsening at 873 K, which contributes to the high saturation magnetization (104.4 emu/g) and low coercivity H_C (151.2 A/m) at this temperature (Fig. 11d). In contrast, the BCC nanoprecipitates coarsen remarkably at 973 K, with the average size increasing from ~ 90 nm in 24-h aged state to ~ 150 nm in 480-h aged state. The coarsening of BCC nanoprecipitates increases the coercivity to 1950 A/m (in 480-h aged state). By contrast, the coarsening of BCC nanoprecipitates in S5- $\text{Al}_3\text{Co}_4\text{Fe}_7\text{Cr}_3$ alloy is very severe. Especially after aging at 1073 K for 24 h, the BCC and B2 phases exhibit a lamellar microstructure with a width of ~ 180 nm (Fig. 10d), which heavily deteriorates the coercivity (1974.1 A/m).

Generally, a large lattice misfit between the BCC nanoprecipitates and B2 matrix tend to accelerate the coarsening of the nanoprecipitates [22], which is not consistent with the observation that the BCC particles coarsen obviously at temperatures above 973 K in the currently developed alloys containing Cr. It may be related to the fast diffusion of Cr at HTs. The diffusion coefficients of Al, Fe, Co, and Cr at different temperatures are listed in Table S3 [36, 41]. Below 973 K, the diffusion coefficients of these elements are relatively low, in a range of $1.40 \times 10^{-21} \sim 3.94 \times 10^{-19} \text{ m}^2 \cdot \text{s}^{-1}$, and the difference among them is not obvious. This contributes primarily to the extremely

low coarsening rate of BCC nanoprecipitates in these alloys. As the aging temperature increases to 973 K and above, the diffusion coefficient of these elements increases significantly. For instance, the diffusion coefficients of Al are 5.72×10^{-18} and $1.14 \times 10^{-16} \text{ m}^2\cdot\text{s}^{-1}$ at 973 and 1073 K, respectively. Thus, the BCC particles in these alloys coarsen considerably. Especially, the diffusion coefficients of Cr ($1.71 \times 10^{-17} \text{ m}^2\cdot\text{s}^{-1}$ at 973 K and $3.74 \times 10^{-16} \text{ m}^2\cdot\text{s}^{-1}$ at 1073 K) are approximately twice that of Al, Fe, and Co, which indicates a fast diffusion of Cr. This would promote the coarsening of the BCC particles significantly. Moreover, the fast diffusion of Cr could result in the formation of composite nanoprecipitates (Fig. 9c), since Cr preferentially enters the interior of the particles while leaving other elements (such as Fe) at the interface between the particles and matrix.

4.2 Microstructure dependence of the coercivity

It is well known that the magnetic properties of an alloy are dependent on the magnetic domains, in which the internal stress induced by crystalline defects could impede the movement of domain walls in an applied magnetic field, leading to an increase in the coercivity [42-44]. Generally, the coercivity is expressed by

$$H_C = \frac{\lambda_s \Delta\sigma}{2\mu_0 M_S \cos\theta} \frac{3\delta/l}{1+3(\delta/l)^2} \quad (1)$$

where λ_s is the magnetostriction coefficient, $\Delta\sigma$ and l are respectively the amplitude and characteristic wavelength of the internal stress field induced by various crystalline defects (especially grain boundaries and ultrafine precipitates), $\mu_0 = 4\pi \times 10^{-7} \text{ N/A}^2$ is the permeability of vacuum, M_S is the saturation magnetization, θ is the angle between the magnetic moment and magnetic field direction after the movement of domain wall, and δ is the width of domain wall. Apparently, the coercivity is closely related to a series of parameters, such as λ_s , M_S , θ , δ , $\Delta\sigma$, and l , which are all dependent on the

microstructure. Among them, the wavelength l is often represented by the grain size D_g in polycrystalline alloys or the interparticle distance λ_p in nanocrystalline alloys, and the domain wall width δ can be estimated by [45, 46]

$$\delta = \pi(A_{ex}/K_1)^{1/2} \quad (2)$$

where $A_{ex} = (k_B T_C)/(2a_0)$ is the exchange stiffness, $k_B = 1.380649 \times 10^{-23}$ J/K is the Boltzmann's constant, T_C is the Curie temperature, a_0 is the lattice parameter of the matrix, and K_1 is the magnetic anisotropy constant [47, 48].

For the S1-Al₃Co₇Fe₇ alloy in both the homogenized and aged states (773 ~ 1073 K), the microstructure consisting of macro-scale equiaxed grains, micro-scale cells, and nano-scale particles is very stable, in which the average grain, cell, and particle sizes are 292 μm , 354 nm, and 4 nm, respectively. Generally, the variation of coercivity with grain size or particle size follows a tendency presented in Fig. 14 [49-51]. When the structural variations occur on a large scale ($D > 100 \mu\text{m}$, larger than the δ) in traditional magnetic alloys, Eq. 1 can be simplified as $H_C \propto 1/D_g$, where the total area and the internal stress induced by grain boundaries would become smaller with increased grain size. While in nanocrystalline alloys, the particle size is much less than the domain wall width. Thus, Eq. 1 can be simplified as $H_C \propto 1/D_p^6$, since the magnetic anisotropy is averaged effectively with several structural units [49]. Only when the grain size is comparable to the domain wall width, the coercivity increases to a maximum (> 3000 A/m), which would render materials with a hard-magnetic feature [49]. According to this tendency, the macro-scale equiaxed grains, micro-scale cells, and nano-scale particles in the S1-Al₃Co₇Fe₇ would produce the coercivity of 2, 1450, and 1 A/m, respectively, as plotted in Fig. 14. Apparently, the experimentally measured values (135~191 A/m) in the homogenized and aged states are largely different from the theoretical values, indicating that the magnetization mechanism is very complex in such

a hierarchical microstructure. Therefore, we need to find a more reasonable way to calculate the coercivity of S1-Al₃Co₇Fe₇ alloy.

The domain wall width was estimated as 211 nm according to Eq. 2 with the input of $a_0 = 0.2870$ nm, $T_C = 1254$ K, and $K_1 = 6.8$ kJ/m³. Here, the value of the magnetic anisotropy constant K_1 was taken from that of binary Co₅₀Fe₅₀ alloy, since the Co/Fe ratio is 1 and the non-ferromagnetic Al does not show any magnetic moment [52]. The characteristic wavelength is equal to the grain/cell size (292 μm and 354 nm, respectively) or the interparticle distance of nanoprecipitates λ_p , which can be calculated by [53]:

$$\lambda_p = \sqrt{2/3}D_p(\sqrt{\pi/4f} - 1) \quad (3)$$

where $f = 10$ % is the volume fraction of BCC nanoparticles determined from the HAADF images (Fig. 5c). Thus, the coercivity values induced by macro-scale equiaxed grains, micro-scale cells, and nano-scale particles are calculated to be $H_{C\text{-macro}}' = 2.6$ A/m, $H_{C\text{-micro}}' = 1026$ A/m, and $H_{C\text{-nano}}' = 33$ A/m, respectively, with the Eq. (1), in which the involved parameters were approximately taken as $\lambda_s = 1 \times 10^{-6}$, $\cos \theta = 1/2$ (the average value), and $\Delta\sigma = 235$ kJ/m³ according to those in traditional Fe-Co-based soft-magnetic alloys [49].

Since the internal stress that impedes the domain wall movement is mainly induced by the interfaces of crystalline defects [42-44], the contributions of the micro-scale grains, micro-scale cells, and nano-scale particles to coercivity of the S1-Al₃Co₇Fe₇ alloy are proportional to their surface areas (S_{macro} , S_{micro} , and S_{nano} , respectively). Thus, the coercivity of the alloy can be calculated by:

$$H_C = A_1 H_{C\text{-macro}}' + A_2 H_{C\text{-micro}}' + A_3 H_{C\text{-nano}}';$$

$$A_1 = \frac{S_{\text{macro}}}{S_T}, A_2 = \frac{S_{\text{micro}}}{S_T}, A_3 = \frac{S_{\text{nano}}}{S_T};$$

$$S_T = S_{macro} + S_{micro} + S_{nano}, S_{macro} = \frac{3V}{D_g}, S_{micro} = \frac{6V}{D_c}, S_{nano} = \frac{6fV}{D_p} \quad (4)$$

where V represents the volume of the bulk alloy, S_T is the total surface area, and $A_1 = 0.0002$, $A_2 = 0.1008$, and $A_3 = 0.89$ are the proportions of S_{macro} , S_{micro} , and S_{nano} to S_T , respectively. Resultantly, the total coercivity was estimated to be 133.5 A/m, which is reasonably consistent with the measured value (135~191 A/m). It is found that the nano-scale particles have made a dominant contribution to the coercivity, while the contribution from the macro-scale grains is very small. Therefore, the low coercivity in S1-Al₃Co₇Fe₇ is primarily ascribed to the uniform distribution of ultrafine ferromagnetic BCC nanoprecipitates.

Similarly, the S3-Al₃Co₆Fe₆Cr₂ alloy exhibits prominent soft-magnetic properties with a low coercivity of 159.2 A/m after aging for 480 h at 873 K due to its stable microstructure. However, after aging for 480 h at 973 K, the coercivity increases to 1950.2 A/m, demonstrating a drastic degradation of soft-magnetic properties. Since the domain wall width was calculated as 192 nm with Eq. 2 ($a_0 = 0.2869$ nm and $T_C = 1052$ K), the coercivity is strongly dependent on the characteristic wavelength l . During aging at 973 K, the sizes of the macro-scale grains do not show significant changes and are comparable to those in the homogenized state, and their contribution to H_C can be neglected, since the ratio of S_{macro} to S_T is less than 0.01. Moreover, the micro-scale cells disappear after aging at 973 K, as shown in Supplementary Fig. S2, indicating that the heat treatment at a relatively high temperature can eliminate the elemental segregation on cell boundaries. Thus, the coercivity values in different states are determined by the BCC nanoprecipitates, which coarsen remarkably after aging at 973 K, increasing from ~ 4 nm in the homogenized state to ~ 90 nm in the 24-h aged state and then to ~ 350 nm (for ellipsoidal particles) in the 480-h aged state. According to Eqs. 1, 3, and 4, the ratio of the coercivity in the aged state to that in the homogenized

state is proportional to $l_{nano} / (l_{nano}^2 + 3\delta^2)$. The calculated coercivity ratios in the 24 - and 480-h aged states to that in the homogenized state are 2.3 and 7.5, respectively, which are comparable to the experimentally measured values, i.e., $270.6 / 143.3 = 1.9$ and $1950.2 / 143.3 = 13.6$, respectively. It is found that the coarsening of BCC nanoparticles increases the contribution of the particle-matrix interface to the coercivity, since the interparticle distance of BCC nanoparticles is much larger than the domain wall width. Especially, when the size of BCC precipitates in 480-h aged state is comparable to or slightly larger than the domain wall width, the coercivity increases drastically. Therefore, it can be deduced that the coherent BCC/B2 microstructure with excellent thermal stability is essential to high-performance soft-magnetic alloys for high-temperature applications, and low coercivity requires the size of BCC nanoprecipitates to be much smaller than the domain wall width.

4.3 Composition dependence of the saturation magnetization and induction intension

The saturation magnetization M_S (or saturation induction intension B_S) depends on the amount of ferromagnetic elements (Fe, Co, and Ni) [18], in which the magnetic moments of Fe, Co, and Ni are 2.2, 1.7, and 0.6 μ_B (Bohr magneton) [54], respectively. The mean magnetic moment per ferromagnetic atom in an alloy can be expressed by $\bar{\mu}_H = \sum \mu_{H,i} \cdot x_i$, where x_i is the amount of element i . For comparison, the B_S and $\bar{\mu}_H$ of several classical soft-magnetic alloys [8, 39, 55-58], such as the Finemet alloy, Hitperm alloy, and other available MPEAs, as well as the currently developed alloys, are listed in Table S4. Figure 14c presents the variation of saturation induction intension with mean magnetic moment per ferromagnetic atom. Obviously, the saturation induction intension shows a linear upward trend with the increased mean magnetic moment per atom, i.e., the increased amount of ferromagnetic elements. In addition, the saturation induction intension (saturation magnetization) values of soft-

magnetic alloys are not susceptible to the crystalline structure, as evidenced by the observation that saturation induction intensity and mean magnetic moment per atom of an FCC-based $\text{Co}_{27.7}\text{Fe}_{32.6}\text{Ni}_{27.7}\text{Ta}_{5.0}\text{Al}_{7.0}$ alloy are comparable to those of the current BCC-based S3- $\text{Al}_3\text{Co}_6\text{Fe}_6\text{Cr}_2$ ($\text{Al}_{17.65}\text{Co}_{35.29}\text{Fe}_{35.29}\text{Cr}_{11.76}$) alloy. It is also noted that the saturation induction intensity values of some alloys (such as $\text{Al}_{1.5}\text{Co}_4\text{Fe}_2\text{Cr}$, Hitperm $\text{Fe}_{44}\text{Co}_{44}\text{Zr}_7\text{B}_4\text{Cu}_1$ alloy, and S1- $\text{Al}_3\text{Co}_7\text{Fe}_7$) are slightly higher than those given by a linear relationship with the mean magnetic moment per atom. It might result from the strong interactions among ferromagnetic atomic pairs in a short range, which could contribute to the magnetic moment per atom of ferromagnetic elements effectively [59].

5. Conclusions

The present work developed a series of novel soft-magnetic MPEAs with a coherent microstructure consisting of ultrafine BCC ferromagnetic nanoprecipitates in the B2 matrix by deliberately tailoring the chemical compositions via the formula of $\text{Al}_3(\text{Co,Fe,Cr})_{14}$. The microstructure and soft-magnetic properties of five representative alloys ($\text{Al}_3\text{Co}_7\text{Fe}_7$, $\text{Al}_3\text{Co}_6\text{Fe}_7\text{Cr}_1$, $\text{Al}_3\text{Co}_6\text{Fe}_6\text{Cr}_2$, $\text{Al}_3\text{Co}_7\text{Fe}_4\text{Cr}_3$, and $\text{Al}_3\text{Co}_4\text{Fe}_7\text{Cr}_3$) were thoroughly studied, and the following conclusions are drawn.

- 1) The MPEAs exhibit excellent soft-magnetic properties with saturation magnetization of 107.4 ~ 167.5 emu/g and coercivity of 143 ~ 303 A/m in the homogenized state, and the increase of Cr content reduces the saturation magnetization gradually. Interestingly, the prominent soft-magnetic properties of the $\text{Al}_3\text{Co}_7\text{Fe}_7$ alloy are not sensitive to the aging temperature (773 ~ 1073 K) and time, as evidenced by the high saturation magnetization (157.9 emu/g) and low coercivity (135.3 A/m) after aging for 480 h at 1073 K. In contrast, the coercivity of $\text{Al}_3\text{Co}_6\text{Fe}_6\text{Cr}_2$ increases slightly with aging temperature, increasing from ~ 150

A/m in the 773 ~ 873-K aged states to 270 ~ 374 A/m in the 973 ~ 1073 K-aged states. The coercivity of the $\text{Al}_3\text{Co}_4\text{Fe}_7\text{Cr}_3$ alloy increases drastically 1974 A/m after aging at 1073 K, which is ascribed to a remarkable change in microstructure.

- 2) The homogenized MPEAs contain ultrafine spherical BCC ferromagnetic nanoparticles with a size of 3 ~ 8 nm in the B2 matrix, which is related to the small lattice misfit ($\varepsilon < 0.21\%$) between the BCC and B2 phases. The BCC/B2 coherent microstructure in the $\text{Al}_3\text{Co}_7\text{Fe}_7$ alloy exhibits the highest thermal stability among the studied alloys, in which the BCC nanoparticles do not coarsen significantly even after aging for 480 h at 1073 K. The BCC nanoparticles are enriched slightly in Co and Fe, compared with the Al-rich B2 matrix. The microstructural stability of BCC/B2 endows the alloy with outstanding soft-magnetic properties at HTs, as presented by saturation magnetization of 134.7 emu/g and coercivity of 167.2 A/m at 973 K.
- 3) The coherent microstructure in the $\text{Al}_3\text{Co}_4\text{Fe}_7\text{Cr}_3$ alloy is also very stable, and the BCC nanoprecipitates do not coarsen significantly after aging for 480 h at 873 K, leading to comparable soft-magnetic properties (saturation magnetization of ~ 130 emu/g and coercivity of ~ 150 A/m) to those in the homogenized state. These ultrafine nanoprecipitates have a core-shell structure, in which Cr partitions to the core and Fe segregates to the shell. Moreover, this alloy exhibits decent HT soft-magnetic properties with saturation magnetization of 104.4 emu/g and coercivity of 151.2 A/m at 873 K. However, further increasing the aging temperature and time leads to an obvious coarsening of BCC particles. The particle size increases to ~ 90 nm after aging at 973 K for 24 h and to ~ 500 nm in length and ~ 190 nm in width (for the short-rod shape) after 480 h aging, which results in a sharply increase of coercivity to ~1950 A/m.

- 4) The analysis on the soft-magnetic mechanisms demonstrates that the coercivity of MPEAs is primarily dependent on the size of BCC nanoprecipitates. When the particle size is comparable to the width of magnetic domain walls (~ 200 nm), the coercivity increases drastically, resulting in a degradation in soft-magnetic property.
- 5) Due to the stable BCC/B2 microstructure, this series of MPEAs have high Curie temperature (1254 K for $\text{Al}_3\text{Co}_7\text{Fe}_7$ and 1052 K for $\text{Al}_3\text{Co}_6\text{Fe}_6\text{Cr}_2$) and electrical resistivity ($262 \sim 285 \mu\Omega\cdot\text{cm}$), showing great potential for HT soft-magnetic applications.

Acknowledgements

It was supported by the National Natural Science Foundation of China (52171152), Research Grant Council of Hong Kong (25202719 and 15227121), and Research Institute for Advanced Manufacturing (P0041364 and P0046108). PKL very much appreciates the support from the National Science Foundation (DMR-1611180, 1809640, and 2226508).

References

- [1] L.K. Varga, Soft magnetic nanocomposites for high-frequency and high-temperature applications, *J. Magn. Magn. Mater.* 316 (2007) 442-447.
- [2] R.T. Fingers, C.S. Rubertus, Application of high temperature magnetic materials, *IEEE Trans. Mag.* 36.5 (2000) 3373-3375.
- [3] W.F. Barret, W. Brown, R.A. Hadffeld, Researches on the electrical conductivity and magnetic properties of upwards of one hundred different alloys of iron, *J. Inst. Electri. Eng.* 156 (1902) 674-722.
- [4] R.S. Sundar, S.C. Deevi, Soft magnetic FeCo alloys: alloy development, processing, and properties, *Int. Mater. Rev.* 50 (2005) 157-192.
- [5] J.S. Blázquez, V. Franco, A. Conde, L. F. Kiss, Soft magnetic properties of high-temperature nanocrystalline alloys: Permeability and magnetoimpedance. *J. Appl. Phys.* 93 (2003) 2172-2177.
- [6] Z. Gercsi, F. Mazaleyrat, L.K. Varga, High-temperature soft magnetic properties of Co-doped nanocrystalline alloys, *J. Magn. Magn. Mater.* 302 (2006) 454-458.
- [7] K.E. Knipling, M. Daniil, M.A. Willard, Fe-based nanocrystalline soft magnetic alloys for high-temperature applications, *Appl. Phys. Lett.* 95 (2009) 222516.
- [8] M.A. Willard, D.E. Laughlin, M.E. McHenry, D. Thoma, K. Sickafus, J.O. Cross, V.G. Harris, Structure and magnetic properties of $(\text{Fe}_{0.5}\text{Co}_{0.5})_{88}\text{Zr}_7\text{B}_4\text{Cu}_1$ nanocrystalline alloys, *J. Appl. Phys.* 84 (1998) 6773-6777.
- [9] Y. Yoshizawa, S. Oguma, K. Yamauchi, New Fe-based soft magnetic alloys composed of ultrafine grain structure, *J. Appl. Phys.* 64 (1988) 6044-6046.
- [10] J.W. Yeh, S.K. Chen, S.J. Lin, J.Y. Gan, T.S. Chin, T.T. Shun, C.H. Tsau, S.Y. Chang, Nanostructured high-entropy alloys with multiple principal elements: Novel alloy design concepts and outcomes. *Adv. Eng. Mater.* 6 (2004) 299-303.

- [11] D.B. Miracle, O.N. Senkov, A critical review of high entropy alloys and related concepts. *Acta Mater.* 122 (2016) 448-511.
- [12] Y.P. Duan, Y.L. Cui, B. Zhang, G.J. Ma, T.M. Wang, A novel microwave absorber of FeCoNiCuAl high-entropy alloy powders: Adjusting electromagnetic performance by ball milling time and annealing. *J. Alloy. Compd.* 773 (2019) 194-201.
- [13] Y. Ma, Q. Wang, X.Y. Zhou, J.M. Hao, B. Gault, Q.Y. Zhang, C. Dong, T.G. Nieh, A novel soft-magnetic B2-based multiprincipal-element alloy with a uniform distribution of coherent body-centered-cubic nanoprecipitates. *Adv. Mater.* 33 (2021) 2006723.
- [14] D. Lan, Z.H. Zhao, Z.G. Gao, K.C. Kou, G.L. Wu, H.J. Wu, Porous high entropy alloys for electromagnetic wave absorption. *J. Magn. Magn. Mater.* 512 (2020) 167065.
- [15] T. Egami, W. Guo, P.D. Rack, T. Nagase, Irradiation resistance of multicomponent alloys, *Metall. Mater. Trans., A.* 45 (2014) 180-183.
- [16] X. Yang, Y.X. Wang, R.N. Min, Z.N. Chen, E.Y. Guo, H.J. Kang, L.W. Li, X. Jiang, T.M. Wang, Enhancement in thermoelectric properties of ZrNiSn-based alloys by Ta doping and Hf substitution, *Acta Mater.* 233 (2022) 117976.
- [17] L.L. Han, F. Maccari, I.R.S. Filho, N.J. Peter, Y. Wei, B. Gault, O. Gutfleisch, Z.M. Li, D. Raabe, A mechanically strong and ductile soft magnet with ultralow coercivity, *Nature* 608 (2022) 310-316.
- [18] G. Herzer, Handbook of magnetic materials, Vol. 10, in: K.H.J. Buschow, (editor), Amsterdam, Elsevier Science BV, 1997.
- [19] S. Huang, W. Li, X.Q. Li, S. Schönecker, L. Bergqvist, E. Holmström, L.K. Varga, L. Vitos, Mechanism of magnetic transition in FeCrCoNi-based high entropy alloys,

- Mater. Des. 103 (2016) 71-74.
- [20] G. Herzer, Modern soft magnets: Amorphous and nanocrystalline materials. *Acta Mater.* 61 (2013) 718-734.
- [21] P.P. Li, A. Wang, C.T. Liu, Composition dependence of structure, physical and mechanical properties of FeCoNi(MnAl)_x, high entropy alloys, *Intermetallics*, , 87(2017) 21-26.
- [22] Y. Ma, Q. Wang, B.B. Jiang, C.L. Li, J.M. Hao, X.N. Li, C. Dong, T.G. Nieh, Controlled formation of coherent cuboidal nanoprecipitates in body-centered cubic high-entropy alloys based on Al₂(Ni,Co,Fe,Cr)₁₄ compositions, *Acta Mater.* 147 (2018) 213-225.
- [23] Q. Wang, Y. Ma, B.B. Jiang, X.N. Li, Y. Shi, C. Dong, P.K. Liaw, A cuboidal B2 nanoprecipitation-enhanced body-centered-cubic alloy Al_{0.7}CoCrFe₂Ni with prominent tensile properties, *Scripta Mater.* 120 (2016) 85-89.
- [24] Q. Wang, J.C. Han, Y.F. Liu, Z.W. Zhang, C. Dong, P.K. Liaw, Coherent precipitation and stability of cuboidal nanoparticles in body-centered-cubic Al_{0.4}Nb_{0.5}Ta_{0.5}TiZr_{0.8} refractory high entropy alloy, *Scripta Mater.* 190 (2021) 40-45.
- [25] D.M. J, Z.H. Wang, J.H. Yuan, B.B. Jiang, F.Y. Yu, J.F. Li, Q. Wang, High-strength and energetic Al₂Ti₆Zr₂Nb₃Ta₃ high entropy alloy containing a cuboidal BCC/B2 coherent microstructure, *J. Alloy. Compd.* 981 (2023) 167546.
- [26] B.D. Cullity, C.D. Graham, *Introduction to magnetic materials*, 2nd edition, Addison Wesley, Boston, 1972.
- [27] Y.F. Kao, T.J. Chen, S.K. Chen, J.W. Yeh, Microstructure and mechanical property of as-cast, -homogenized, and -deformed Al_xCoCrFeNi (0 ≤ x ≤ 2) high entropy alloys, *J. Alloys Compd.* 488 (2009) 57-64.

- [28] Y. Ma, B.B. Jiang, C.L. Li, Q. Wang, C. Dong, P.K. Liaw, F. Xu, L. Sun, The BCC/B2 morphologies in AlxNiCoFeCr high-entropy alloys, *Metals*. 7 (2017) 57.
- [29] D.B. Cullity, S.R. Stock, *Elements of X-Ray Diffraction*, third ed., Prentice Hall, America, 2001.
- [30] J.M. Sosa, J.K. Jensen, D.E. Huber, G.B. Viswanathan, M. A. Gibson, H. L. Fraser, Three-dimensional characterization of the microstructure of an high entropy alloy using STEM/HAADF tomograph, *Mater. Sci. Technol.* 31 (2015) 1250-1258.
- [31] K. Thompson, D. Lawrence, D.J. Larson, J.D. Olson, T.F. Kelly, B. Gorman, In situ site-specific specimen preparation for atom probe tomography, *Ultramicroscopy* 107 (2007) 2-3.
- [32] B. Gault, M. Moody, F. de Geuser, G. Tsafnat, A. La Fontaine, L. Stephenson, D. Haley and S. Ringer: Advances in the calibration of atom probe tomographic reconstruction *Journal of Applied Physics*. 105 (2009) 034913.
- [33] J.Y. He, H. Wang, H.L. Huang, X.D. Xu, M.W. Chen, Y. Wu, X.J. Liu, T.G. Nieh, K. An, Z.P. Lu, A precipitation-hardened high-entropy alloy with outstanding tensile properties, *Acta Mater.* 102 (2016) 187-196.
- [34] Z.Y. Ji, Q. Wang, Z.H. Wang, Y.P. Duan, C. Dong, P.K. Liaw, Electromagnetic wave-absorbing behavior of soft-magnetic medium entropy alloys with BCC/L2₁ coherent microstructure, *Mater. Des.* 222(2022) 111054.
- [35] ASM International Alloy Phase Diagram and the Handbook Committees, *ASM Handbook, Alloy phase diagrams*. ASM International. 13B, 1992.
- [36] Z.Q. Sun, P.D. Edmondson, Y. Yamamoto, Effects of Laves phase particles on recovery and recrystallization behaviors of Nb-containing FeCrAl alloys, *Acta Mater.* 144 (2018) 716–727.
- [37] H. F. Sun, W. J. Qiang, *Magnetic Functional Materials*, Chemistry Industry Press,

Beijing, China 2007.

- [38] P.P. Li, A. Wang, C.T. Liu, A ductile high entropy alloy with attractive magnetic properties, *J. Alloys Compd.* 694 (2017) 55-60.
- [39] D.W. Dietrich, in *Properties and selection: nonferrous alloys and special-purpose materials*, Vol 2, ASM Handbook, (Ed: ASM International Handbook committee), ASM International, USA 1992, p 761.
- [40] G. Herzer, Modern soft magnets: Amorphous and nanocrystalline materials, *Acta Mater.* 61 (2013) 718-734.
- [41] H. Nitta, T. Yamamoto, R. Kanno, K. Takasawa, T. Iida, Y. Yamazaki, Diffusion of molybdenum in α -iron, *Acta Mater.* 50 (2002) 4117-4125.
- [42] S. Ogu, Y. Iijim, G. Herzer, in *Handbook of magnetic materials*, Vol. 10 (Ed: K. H. J. Buschow), Elsevier Science BV, Amsterdam, the Netherlands, 1997.
- [43] W.D. Zhong, *Ferro magnetics*, Science Press, Beijing, China 1987.
- [44] F.E. Luborsky, J.D. Livingston, G.Y. CHIN, in *Physical Metallurgy*, Vol. 3 (Eds: R. W. Cahn, P. Haasen), Elsevier Science BV, Amsterdam, the Netherlands, 1996, Ch. 29.
- [45] L. Néel, *Ann. Univ. Grenoble.* 22 (1946) 299-343.
- [46] F. Pfeifer, C. Radloff, Soft magnetic Ni-Fe and Co-Fe alloys - some physical and metallurgical aspects, *J. Magn. Magn. Mater.* 19 (1980) 190-207.
- [47] W. D. Callister Jr, D. G. Rethwisch, *Fundamentals of materials science and engineering: an integrated approach.*
- [48] J. Roesler. *Mechanical behaviour of engineering materials: metals, ceramics, polymers, and composites.* (Springer, 1st ed., New York, 2007).
- [49] G. Herzer, Modern soft magnets: Amorphous and nanocrystalline materials, *Acta Mater.* 61 (2013) 718-734.

- [50] F. E. Luborsky, P. Arthur, N.L. Cox, J.N. Ingraham, A.L. Oppergard, M.S. Sadler
Synthesis and properties of ferromagnetic chromium oxide, *J. Appl. Phys.* 32 (1961)
S374-375.
- [51] W.D. Zhong, *Ferromagnetism*, Science Press, Beijing, China 1987.
- [52] L.W. McKeehan. Ferromagnetic anisotropy in nickel-cobalt-iron crystals at various
temperatures. *Phys. Rev.* 51 (1937) 136-139.
- [53] W.F. Hosford, *Mechanical Behavior of Materials*, Cambridge University Press,
New York, 2005 first ed..
- [54] B. D. Cullity, C. D. Graham, *Introduction to magnetic materials*, Addison Wesley,
Boston, USA 1972.
- [55] Y. Zhang, T. T. Zuo, Y. Q. Cheng, P. K. Liaw, High-entropy alloys with high
saturation magnetization and electrical resistivity and malleability, *Sci. Rep.* 3
(2013) 1455.
- [56] T. T. Zuo, R. B. Li, X. J. Ren, Y. Zhang, Effects of Al and Si addition on the
structure and properties of CoFeNi equal atomic ratio alloy, *J. Magn. Magn. Mater.*
371 (2014) 60-68.
- [57] Y. Yoshizawa, S. Oguma, K. Yamauchi, New Fe-based soft magnetic alloys
composed of ultrafine grain structure, *J. Appl. Phys.* 64 (1988) 6044-6046.
- [58] K. Suzuki, A. Makino, A. Inoue, T. Masumoto, Amorphous Fe-B-Si magnetic films
by reactive sputtering from a pure iron source, *J. Appl. Phys.* 70 (1991) 6232-6235.
- [59] S. Huang, W. Li, X. Q. Li, S. Schönecker, L. Bergqvist, E. Holmström, L. K. Varga,
L. Vitos, Mechanism of magnetic transition in FeCrCoNi-based high entropy alloys,
Mater. Des. 103 (2016) 71-74.

Figure Captions

Fig. 1 — RT hysteresis loops of the $\text{Al}_3(\text{Co,Fe,Cr})_{14}$ MPEAs in different states: (a) S1 ~ S5 in the homogenized state, (b) S1 after aging at 773 ~ 1073 K, (c) S3 after aging at 773 ~ 1073 K, and (d) S5 after aging at 773 ~ 1073 K.

Fig. 2 — (a) XRD patterns of the homogenized S1 ~ S5 alloys and (b) variations of lattice constants of the BCC and B2 phases and lattice misfits between them in the S1 ~ S5 alloys.

Fig. 3 — Microstructural characterization of the S1 and S3 alloys in the as-homogenized state: EBSD IPF maps of the (a) S1- $\text{Al}_3\text{Co}_7\text{Fe}_7$ and (b) S3- $\text{Al}_3\text{Co}_6\text{Fe}_6\text{Cr}_2$ alloys, showing coarse macro-scale equiaxed grains, SEM images of the (c) S1 and (d) S3 alloys, showing micro-scale cells in each equiaxed grain, (e) DF-TEM image and the corresponding SAED pattern of the S3 alloy, and (f) HRTEM image and FFT patterns along the [100] direction of the S3 alloy.

Fig. 4 — SEM micrographs of the aged S1- $\text{Al}_3\text{Co}_7\text{Fe}_7$ alloy in different aged states: (a) 24 h at 773 K, (b) 24 h at 873 K, (c) 480 h at 973 K, and (d) 480 h at 1073 K.

Fig. 5 — TEM characterization of the aged S1- $\text{Al}_3\text{Co}_7\text{Fe}_7$ alloy in different aged states: (a) TEM-DF image and corresponding SAED pattern along $[110]_{\text{BCC}}$ direction of the alloy aged at 773 K for 24 h showing the precipitation of ultrafine BCC nanoparticles in the L_{21} matrix, (b) the TEM-DF image and corresponding SAED pattern of the alloy aged at 1073 K for 480 h showing the precipitation of ultrafine BCC nanoparticles in the B2 matrix, (c) HAADF image of the alloy aged at 1073 K for 480 h showing BCC nanoparticles with sizes of 3 ~ 5 nm, and (d) chemical compositions of BCC nanoparticles and B2 matrix by TEM-EDS.

Fig. 6 — APT characterization of the S1- $\text{Al}_3\text{Co}_7\text{Fe}_7$ alloy aged at 1073 K for 480 h: (a) atom maps of Al, Co, and Fe, (b) the concentration isosurface of 44 at. % Co showing

the distribution of ultrafine BCC nanoparticles in the B2 matrix, and (c) corresponding proximity histogram based on the concentration isosurface showing that Al and Fe are enriched in the B2 matrix and Co partitions to the BCC nanoparticles.

Fig. 7 — SEM observations of the S3-Al₃Co₆Fe₆Cr₂ alloy aged at 973 K for (a) 24 and (b) 480 h showing the obvious coarsening of BCC nanoparticles.

Fig. 8 — HAADF-STEM micrograph and corresponding EDS mapping of the S3-Al₃Co₆Fe₆Cr₂ alloy aged at 973 K for 480 h, showing that the BCC nanoprecipitates are enriched in Cr and Fe, while the B2 matrix is segregated by Al and Co.

Fig. 9 — APT characterization of the S3-Al₃Co₆Fe₆Cr₂ alloy aged at 773 K for 24 h: (a) atom maps for Al, Cr, Fe, and Co, (b) an enlarged view of the precipitates depicted with the concentration isosurface of 25 at. % Cr and 39 at. % Fe overlaid on top of the atom map, showing that the BCC nanoparticles are enriched in Cr and surrounded by Fe to form a core-shell structure, and (c) corresponding proximity histogram generated from all the nanoprecipitates, showing that Al, Fe, and Co are enriched in B2 matrix and Cr is segregated in the BCC nanoparticles.

Fig. 10 — SEM micrographs of the S5-Al₃Co₄Fe₇Cr₃ alloy after aging for 24 h at different temperatures: (a) 773 K, (b) 873 K, (c) 973 K, and (d) 1073 K.

Fig. 11 — Thermomagnetic curves of the homogenized (a) S1-Al₃Co₇Fe₇ and (b) S3-Al₃Co₆Fe₆Cr₂ alloys, in which the Curie temperature can be obtained, and HT hysteresis loops at 773 ~ 973 K of the (c) S1 and (d) S3 alloys after aging at 973 K for 480 h.

Fig. 12 — (a) Electrical resistivity of the homogenized MPEAs at RT, and (b) variation of electrical resistivity of the S3-Al₃Co₆Fe₆Cr₂ alloy with temperature (from RT to 1078 K).

Fig. 13 — (a) Comparisons of resistivity (ρ) and Curie temperature (T_C) of the currently developed alloys with conventional soft-magnetic alloys, (b) B_S versus H_C of the

currently developed alloys and conventional soft-magnetic materials, where those of the current alloys are also marked with stars, and (c) variation of B_s with the mean magnetic moment per atom ($\bar{\mu}_H$).

Fig. 14 — Variation of the coercivity (H_C) with grain size or particle size of different soft-magnetic materials, in which the H_C values of the macro-scale equiaxed grains, sub-microscale cells, and nano-scale particles in the S1- $\text{Al}_3\text{Co}_7\text{Fe}_7$ alloy are plotted.

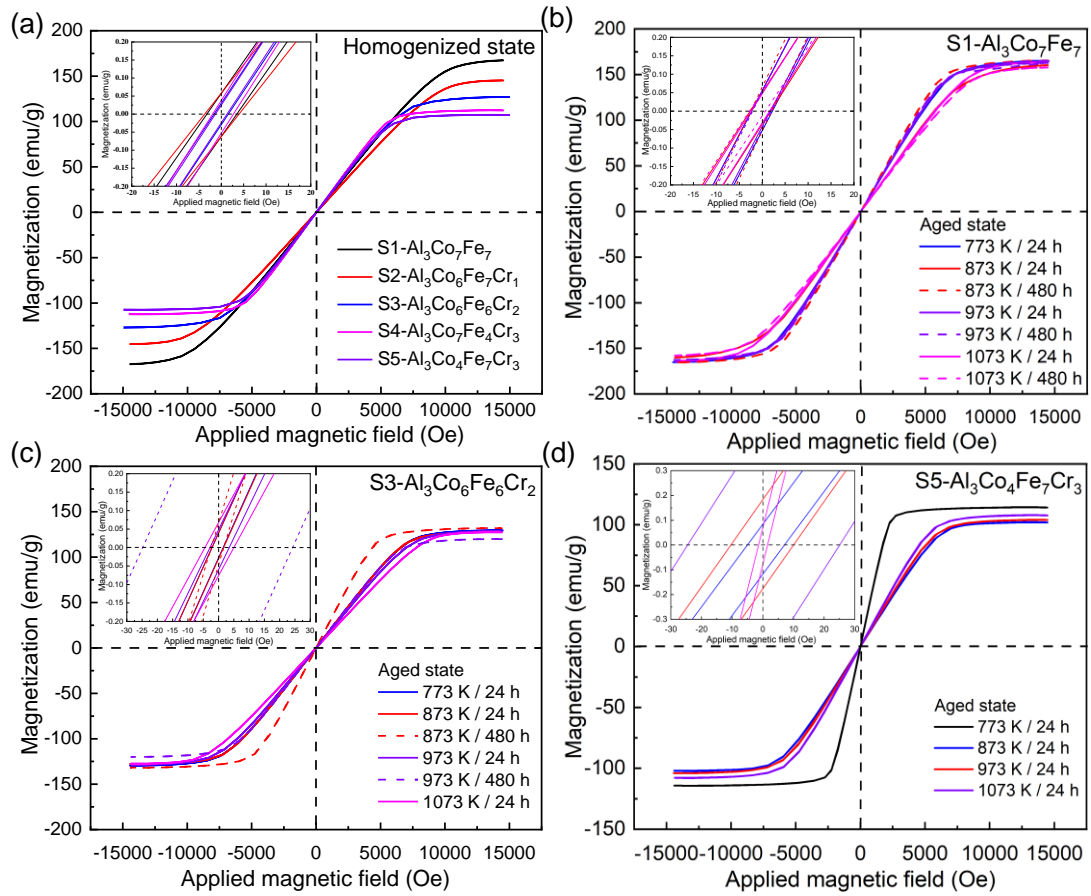


Fig. 1 RT hysteresis loops of the $\text{Al}_3(\text{Co,Fe,Cr})_{14}$ MPEAs in different states: (a) S1 ~ S5 in the homogenized state, (b) S1 after aging at 773 ~ 1073 K, (c) S3 after aging at 773 ~ 1073 K, and (d): S5 after aging at 773 ~ 1073 K.

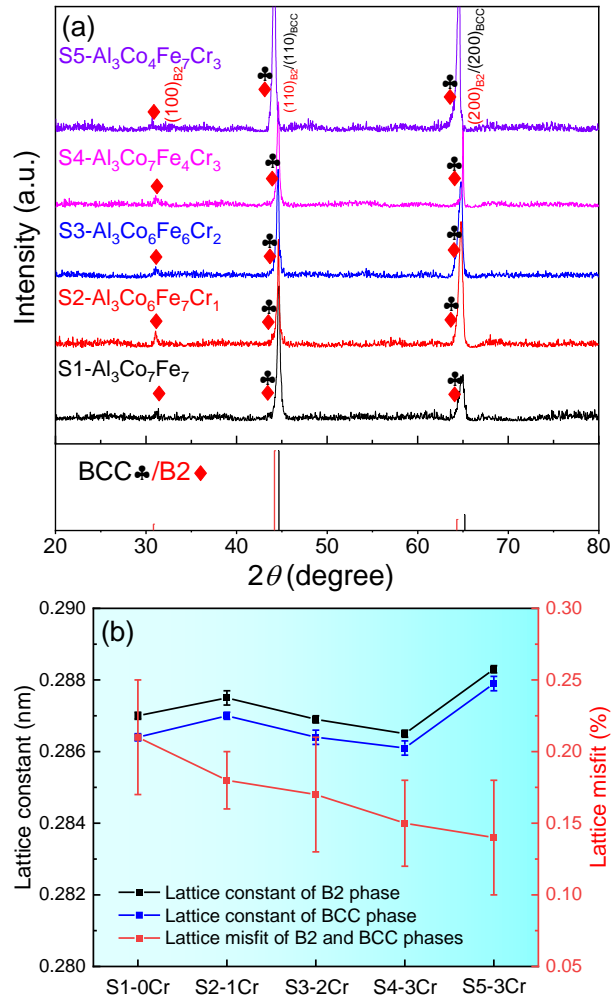


Fig. 2 (a) XRD patterns of the homogenized S1 ~ S5 alloys and (b) variations of lattice constants of the BCC and B2 phases and lattice misfits between them in the S1 ~ S5 alloys.

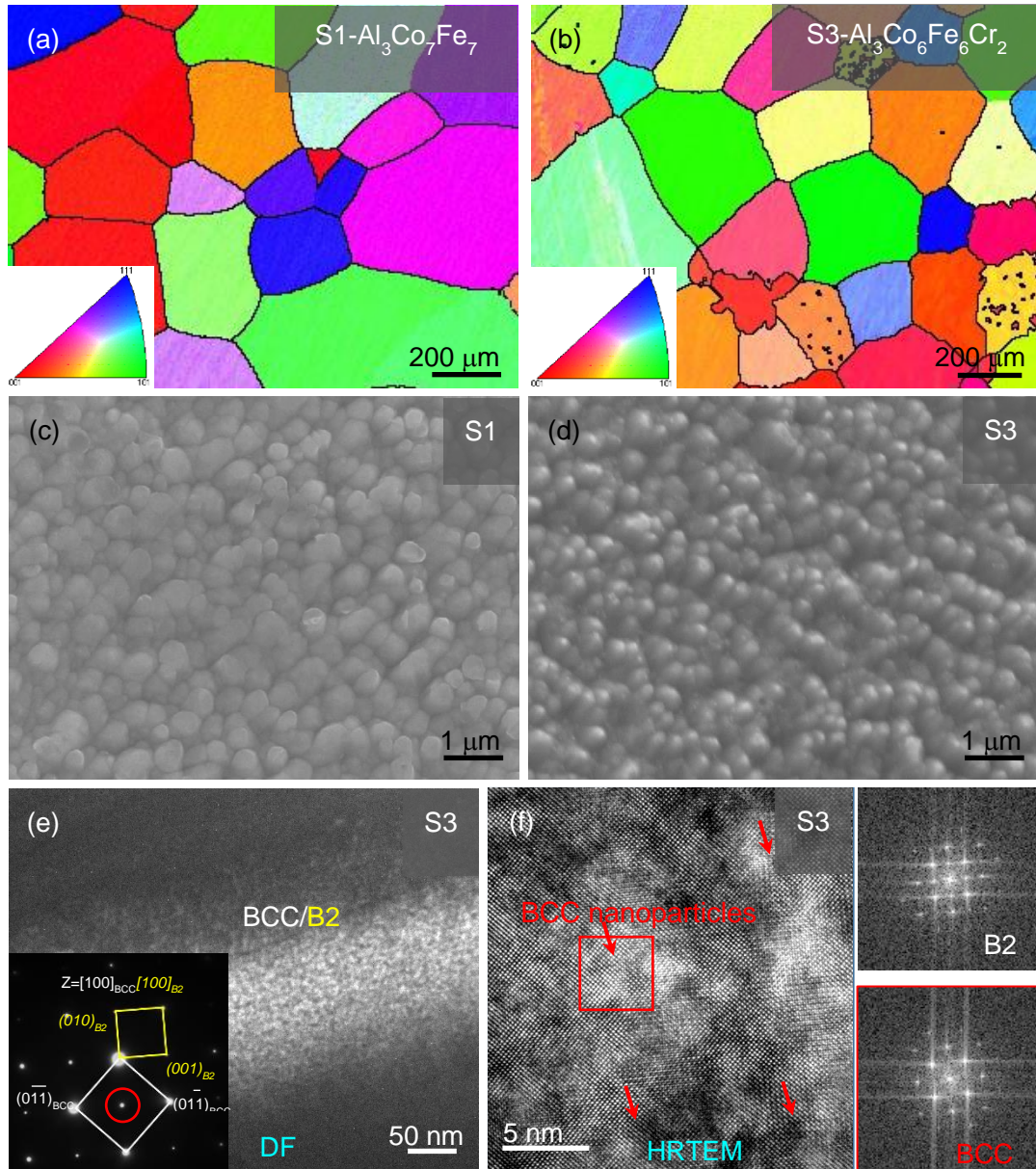


Fig. 3 Microstructural characterization of the S1 and S3 alloys in the as-homogenized state: EBSD IPF maps of the (a) S1-Al₃Co₇Fe₇ and (b) S3-Al₃Co₆Fe₆Cr₂ alloys, showing coarse macro-scale equiaxed grains, SEM images of the (c) S1 and (d) S3 alloys, showing micro-scale cells in each equiaxed grain, (e) DF-TEM image and the corresponding SAED pattern of the S3 alloy, and (f) HRTEM image and FFT patterns along the [100] direction of the S3 alloy.

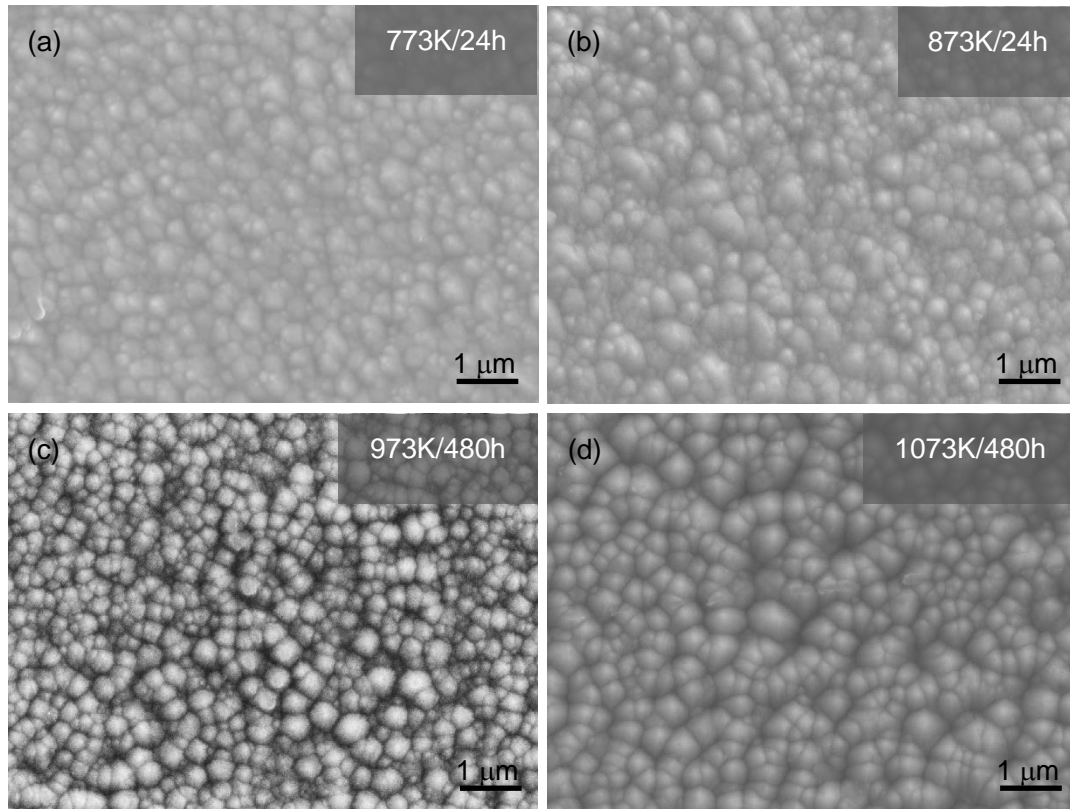


Fig. 4 SEM micrographs of the aged S1-Al₃Co₇Fe₇ alloy in different aged states: (a) 24 h at 773 K, (b) 24 h at 873 K, (c) 480 h at 973 K, and (d) 480 h at 1073 K.

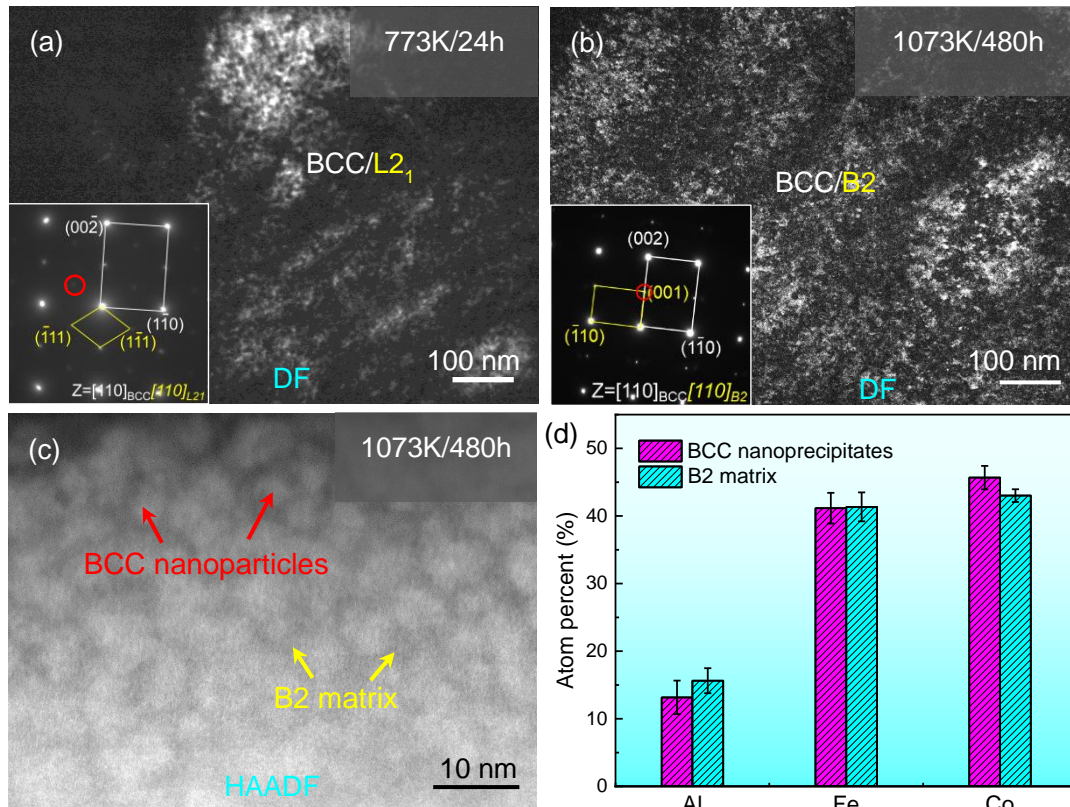


Fig. 5 TEM characterization of the aged S1-Al₃Co₇Fe₇ alloy in different aged states: (a) TEM-DF image and corresponding SAED pattern along [110]_{BCC} direction of the alloy aged at 773 K for 24 h showing the precipitation of ultrafine BCC nanoparticles in the L₂₁ matrix; (b) the TEM-DF image and corresponding SAED pattern of the alloy aged at 1073 K for 480 h showing the precipitation of ultrafine BCC nanoparticles in the B₂ matrix, (c) HAADF image of the alloy aged at 1073 K for 480 h showing BCC nanoparticles with sizes of 3 ~ 5 nm, and (d) chemical compositions of BCC nanoparticles and B₂ matrix by TEM-EDS.

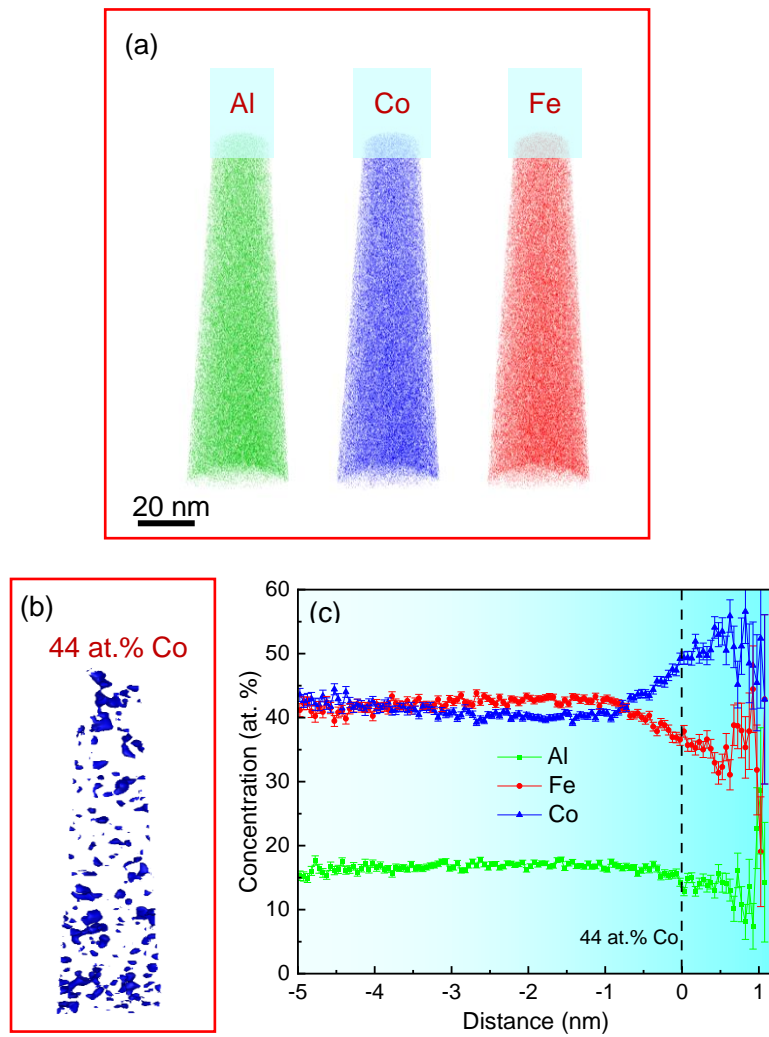


Fig. 6 APT characterization of the S1-Al₃Co₇Fe₇ alloy aged at 1073 K for 480 h: (a) atom maps of Al, Co, and Fe, (b) the concentration isosurface of 44 at. % Co showing the distribution of ultrafine BCC nanoparticles in the B2 matrix, and (c): corresponding proximity histogram based on the concentration isosurface showing that Al and Fe are enriched in the B2 matrix and Co partitions to the BCC nanoparticles.

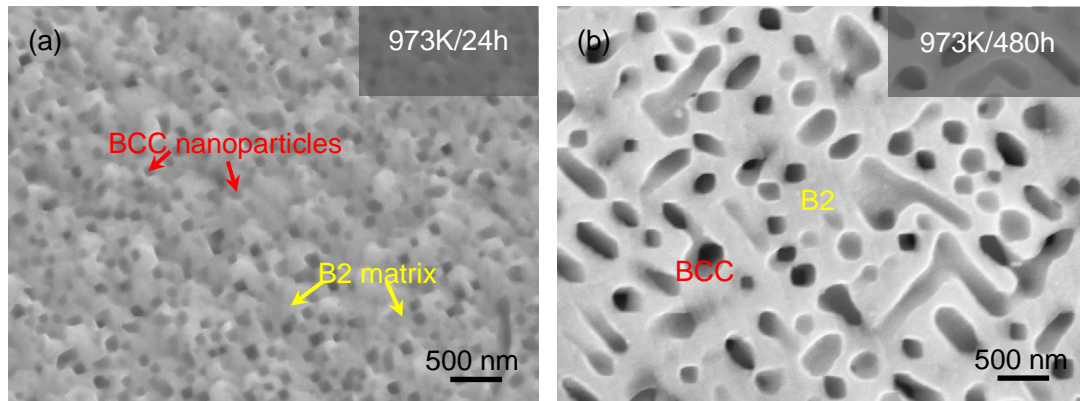


Fig. 7 SEM observations of the S3-Al₃Co₆Fe₆Cr₂ alloy aged at 973 K for (a) 24 and (b) 480 h showing the obvious coarsening of BCC nanoparticles.

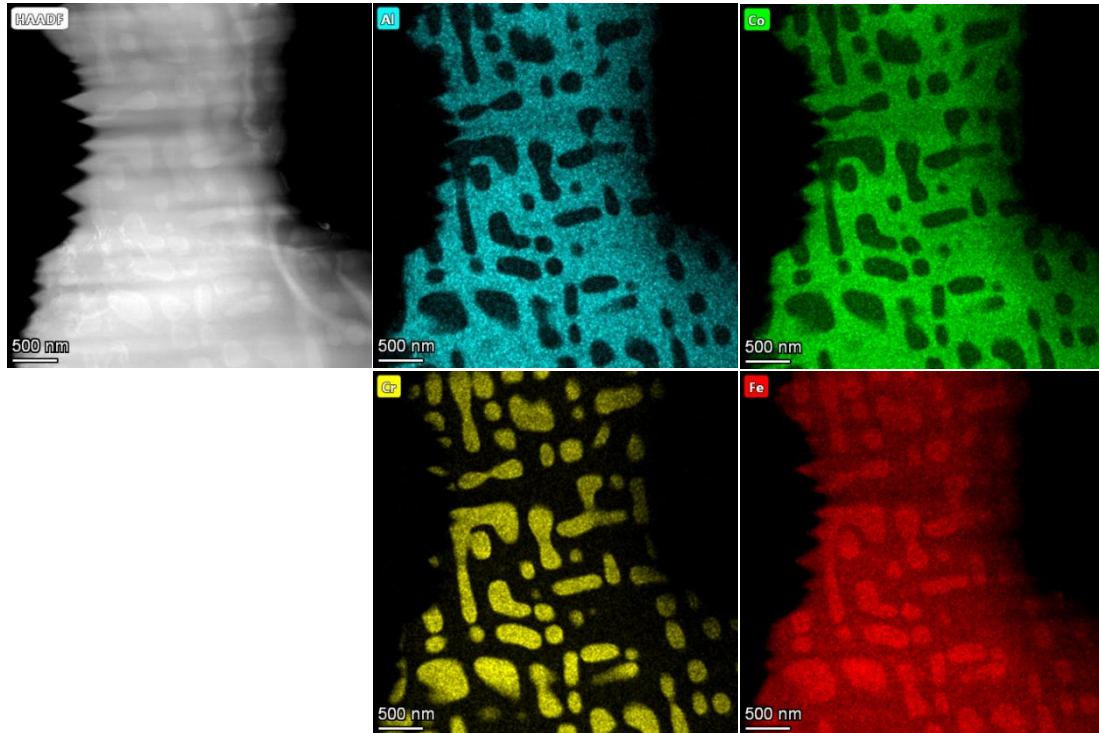


Fig. 8 HAADF-STEM micrography and corresponding EDS mapping of the S3- $\text{Al}_3\text{Co}_6\text{Fe}_6\text{Cr}_2$ alloy aged at 973 K for 480 h, showing that the BCC nanoprecipitates are enriched in Cr and Fe, while the B2 matrix is segregated by Al and Co.

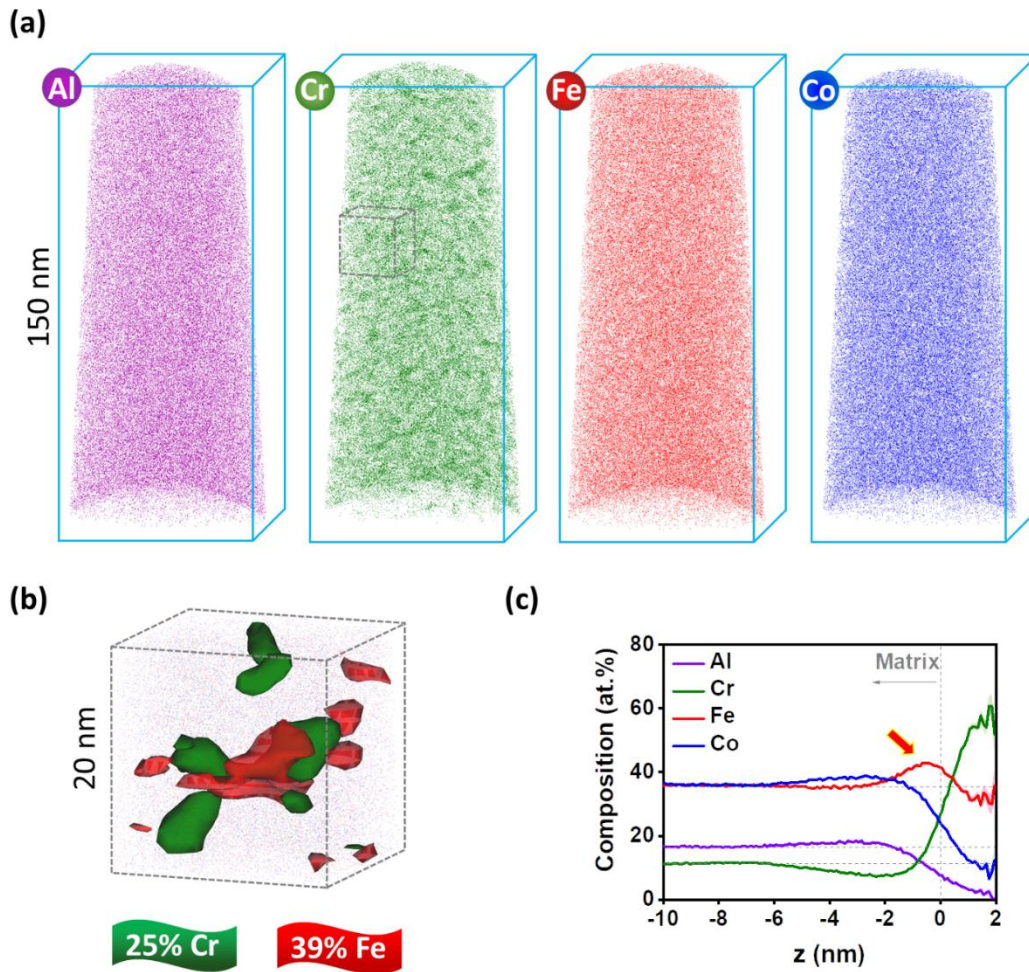


Fig. 9 APT characterization of the S3- $\text{Al}_3\text{Co}_6\text{Fe}_6\text{Cr}_2$ alloy aged at 773 K for 24 h: (a) atom maps for Al, Cr, Fe, and Co. (b): an enlarged view of the precipitates depicted with the concentration isosurface of 25 at. % Cr and 39 at. % Fe overlaid on top of the atom map, showing that the BCC nanoparticles are enriched in Cr and surrounded by Fe to form a core-shell structure, and (c) corresponding proximity histogram generated from all the nanoprecipitates, showing that Al, Fe, and Co are enriched in B2 matrix and Cr is segregated in the BCC nanoparticles.

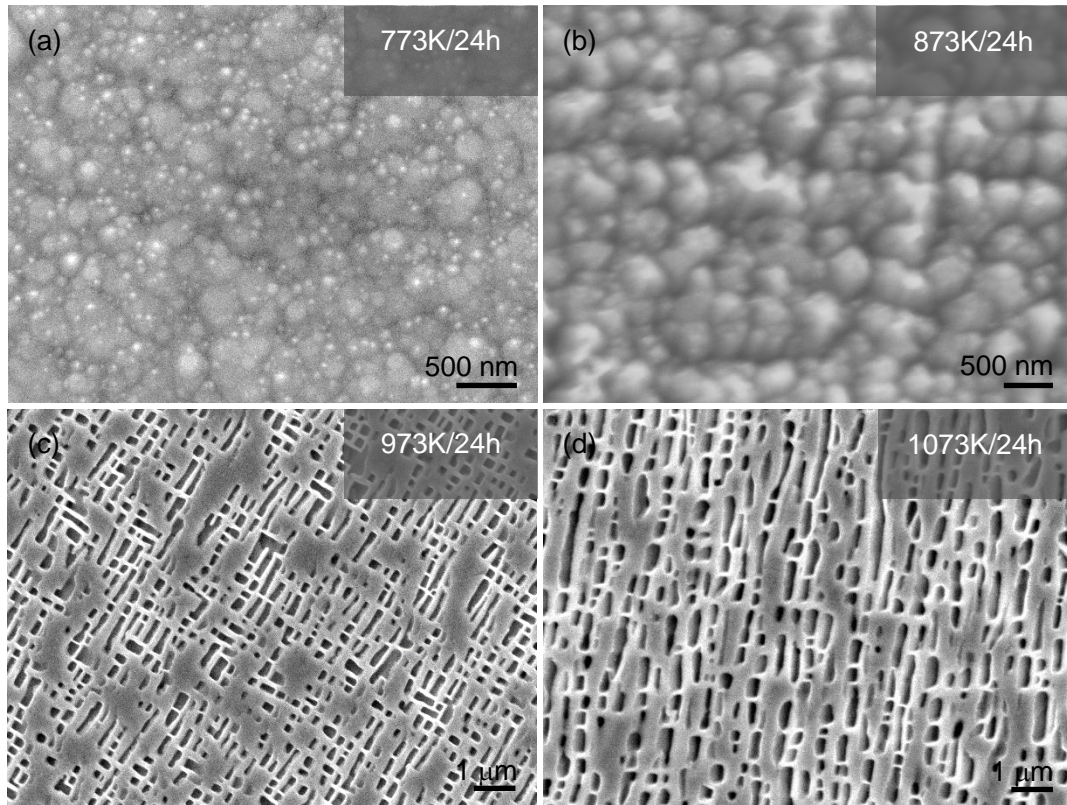


Fig. 10 SEM micrographs of the S5-Al₃Co₄Fe₇Cr₃ alloy after aging for 24 h at different temperatures: (a) 773 K, (b) 873 K, (c) 973 K, and (d) 1073 K.

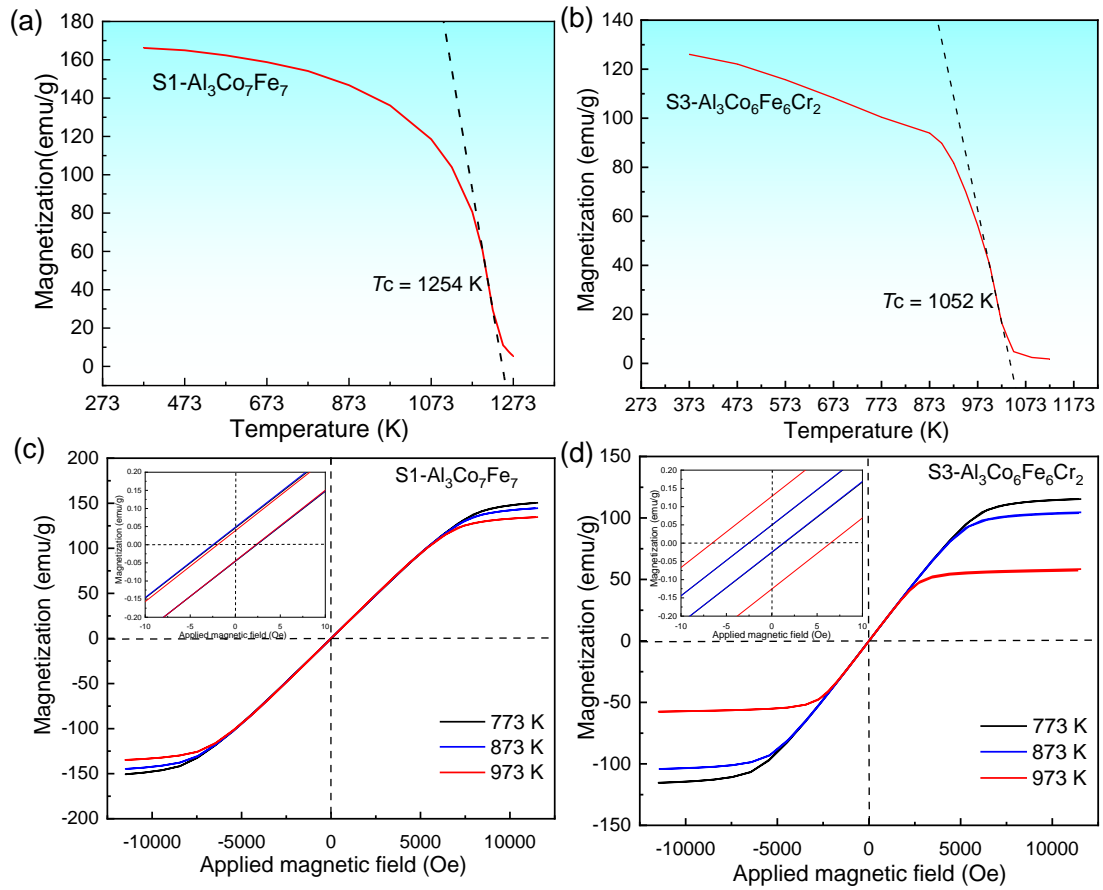


Fig. 11 Thermomagnetic curves of the homogenized (a) S1-Al₃Co₇Fe₇ and (b) S3-Al₃Co₆Fe₆Cr₂ alloys, in which the Curie temperature can be obtained, and HT hysteresis loops at 773 ~ 973 K of the (c) S1 and (d) S3 alloys after aging at 973 K for 480 h.

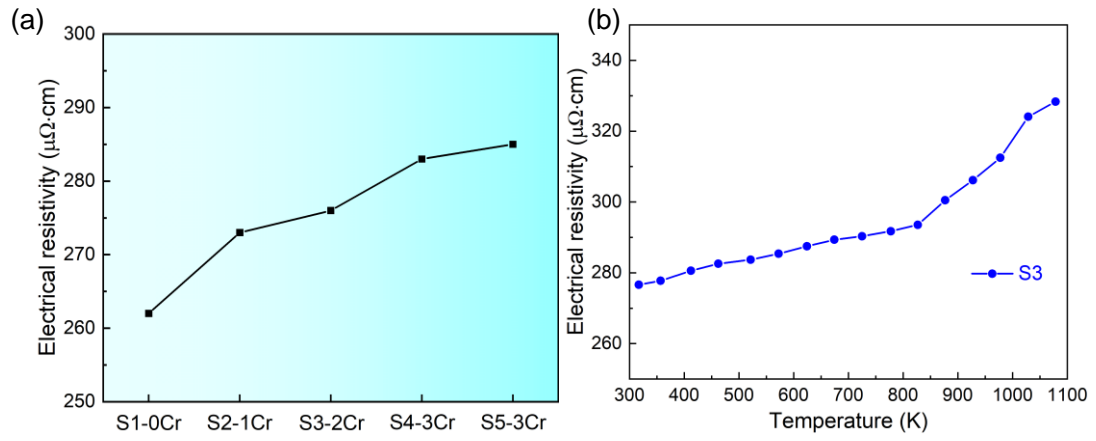


Fig. 12 (a): Electrical resistivity of the homogenized MPEAs at RT, and (b) variation of electrical resistivity of the S3- $\text{Al}_3\text{Co}_6\text{Fe}_6\text{Cr}_2$ alloy with temperature (from RT to 1078 K).

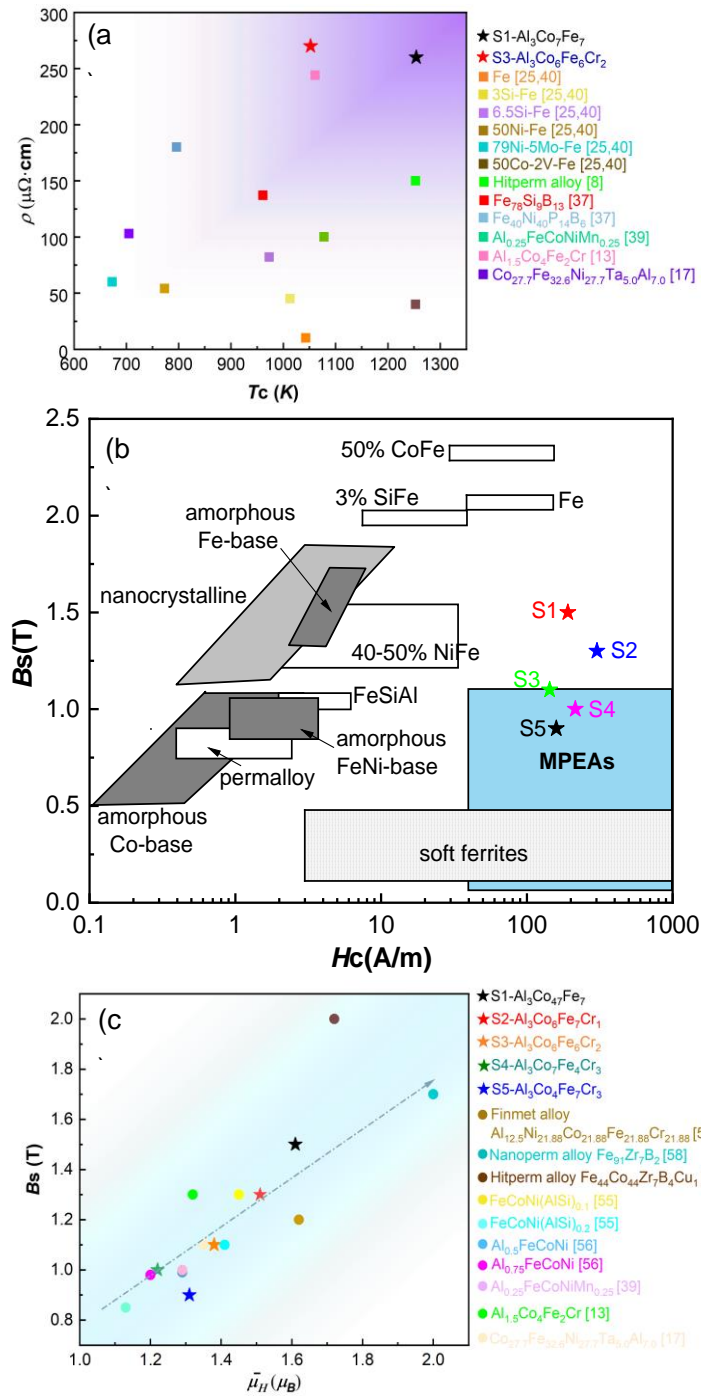


Fig. 13 (a): Comparisons of resistivity (ρ) and Curie temperature (T_c) of the currently developed alloys with conventional soft-magnetic alloys, (b): B_s versus H_c of the currently developed alloys and conventional soft-magnetic materials, where those of the current alloys are also marked with stars, and (c) variation of B_s with the mean magnetic moment per atom ($\bar{\mu}_H$).

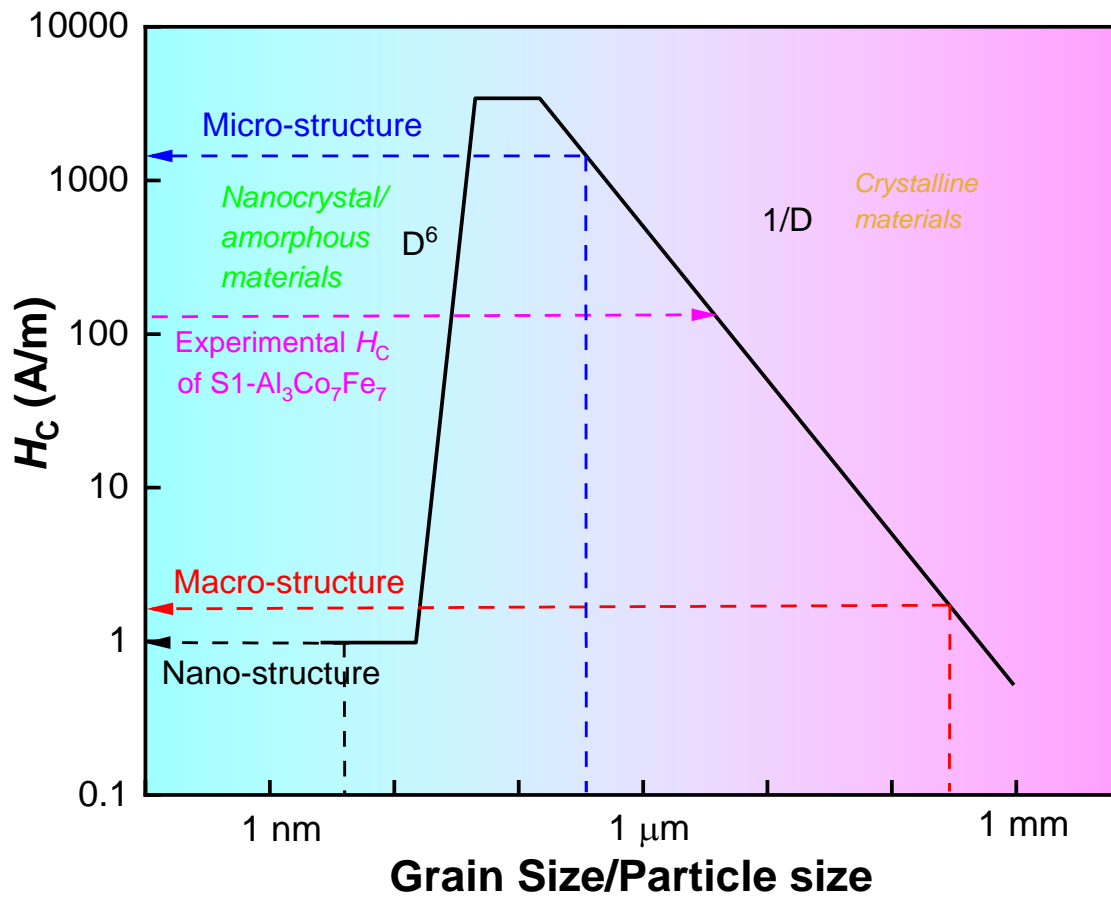


Fig. 14 Variation of the coercivity (H_C) with grain size or particle size of different soft-magnetic materials, in which the H_C values of the macro-scale equiaxed grains, sub-microscale cells, and nano-scale particles in the S1-Al₃Co₇Fe₇ alloy are plotted.